Advanced Functional Materials

ADVANCED FUNCTIONAL MATERIALS
www.afm-journal.de

RESEARCH ARTICLE

Tuning Viscoelasticity of Dynamic Covalent Hydrogels for Human Tissue Modeling

Narelli de Paiva Narciso[1] | Fotis Christakopoulos[1] | Michelle S. Huang[2,3] | Neil J. Baugh[1] | Carla Huerta-López[1] | Eliana X. Matos[1] | Kristine P. Pashin[1] | Andrew J. Spakowitz[2] | Sarah C. Heilshorn[1]

[1]Department of Materials Science and Engineering, Stanford University, Stanford, California, USA | [2]Department of Chemical Engineering, Stanford University, Stanford, California, USA | [3]The Institute for Chemistry, Engineering & Medicine for Human Health (Sarafan CheM-H), Stanford University, Stanford, California, USA

Correspondence: Sarah C. Heilshorn (heilshorn@stanford.edu)

Received: 12 December 2025 | **Revised:** 3 May 2026 | **Accepted:** 29 May 2026

Keywords: DCC chemistry | dynamic hydrogels | neural progenitor cells | stress-relaxation

ABSTRACT

The development of three-dimensional (3D) in vitro tissue culture models is critical for biomedical research. Hydrogel-based systems have become preferred scaffolds for 3D models, as they have tunable viscoelastic properties, which are well-known to influence cell morphology and function. Particularly, reversible hydrogel crosslinks formed through dynamic covalent chemistry (DCC) can introduce viscoelastic behavior including stress relaxation. However, traditional strategies to increase relaxation rates in DCC gels rely on faster bond kinetics, resulting in faster erosion rates that prevent their use for long-term 3D culture. As an alternative strategy, we explore the use of molecular parameters (specifically molecular weight and degree of functionalization) to carefully control hydrogel stiffness and stress relaxation behavior, creating different combinations of mechanics, while preventing rapid erosion. To aid in interpreting our measurements, we develop and validate a modified theoretical model of gel viscoelasticity to account for additional relaxation process, applying it to a two-component DCC gel composed of modified hyaluronic acid and elastin-like protein. Finally, we utilize this tunable gel platform to explore the impact of scaffold viscoelasticity on encapsulated human neural progenitor cells. In summary, this work expands the molecular design space of DCC hydrogels to achieve tunable viscoelastic properties for 3D in vitro models.

1 | Introduction

The development of in vitro tissue culture models has been paramount in biomedical research, as they allow mechanistic studies with carefully controlled variables, hold potential for high-throughput screening, and reduce our reliance on animal models [1–4]. Thus, there is a growing interest in so-called "new approach methodologies" (i.e., NAMs) such as organ-on-a-chip systems, 3D cell culture models, and patient-derived organoids that can improve our understanding of human development, disease progression, drug discovery, and regenerative medicine [4–11]. However, a central challenge in the field is the ability to reproducibly emulate the complex biomechanical and biochemical environment of native tissue matrices [1, 11, 12].

One of the key challenges is mimicking the viscoelastic mechanical properties of natural tissue, which present a time-dependent response to stress and deformation that can be exerted either by cells or by external stimuli [12–16]. The importance of mechanical cues to guide cell behavior has been widely reported, impacting stem cell differentiation, cell migration, morphology, and proliferation, among other processes [16–22]. More recently, the importance of the kinetics of stress relaxation (a characteristic of viscoelastic materials) has been highlighted, in addition to

the more traditionally studied stiffness (storage modulus, G') [12, 13, 22–24]. Both stiffness and stress relaxation rate can significantly change across different tissues and different stages of development or disease progression, impacting cell behavior [13, 24]. As a consequence, hydrogels have risen to prominence as ideal in vitro systems for studies of cellular biomechanics due to their tunable mechanical properties [1, 2].

While the effects of hydrogel stiffness on cellular behavior have been extensively explored [17–21, 25], studies on the consequences of different stress relaxation rates, especially in combination with varied stiffness, are less common. A key reason for this constraint is the inherent difficulty of independently tuning stiffness and stress relaxation kinetics within a cell-compatible hydrogel. Moreover, fast stress-relaxing hydrogels tend to suffer from rapid erosion profiles (often on the order of 1–3 days), preventing longer cell culture times [26, 27].

Our group has previously utilized recombinant biopolymers and dynamic covalent chemistry (DCC) to achieve hydrogels with tunable stiffness, stress relaxation rate, injectability, and cell-instructive domains [28–31]. These materials are formed through a recombinant elastin-like protein (ELP) and recombinant hyaluronic acid (HA), which together we term HELP gels. Recombinant biopolymers offer the advantages of being biodegradable and cell-interactive (similar to native biopolymers) while also being reproducible and synthesized with animal-free methods (similar to synthetic polymers) [28, 32–34]. The ELP protein incorporates alternating blocks of repetitive elastin-like peptides that provide mechanical elasticity and cell-interactive sequences derived from fibronectin that provide adhesion to integrin cell-surface receptors [31, 32]. HA is one of the main extracellular matrix (ECM) components throughout the human body and can be chemically functionalized through bioorthogonal chemistry [18, 35, 36]. The use of recombinant HA of specific molecular weights allows us to explore the role of molecular parameters in dictating macroscale hydrogel mechanics.

A commonly reported method to achieve DCC hydrogels with tunable stress relaxation rates is to select crosslinks with varying on-and-off rate kinetics [26, 37–41]. While successful, these strategies also affect other hydrogel characteristics that are crucial for in vitro modeling, such as gelation time [42] and erosion kinetics [26]. When gelation time is too rapid or too slow, this can prevent homogeneous cell encapsulation, and when erosion is too rapid, this can prevent long-term cell culture. As an alternative approach, we hypothesized that molecular manipulation of the polymer molecular weight and/or degree of functionalization would enable formulation of DCC hydrogels with tunable control of stiffness and stress relaxation rate.

To test this hypothesis, we synthesize a large family of recombinant HELP hydrogels crosslinked through hydrazone DCC. Through experimental rheological analysis and theoretical modeling, we identify the molecular design parameters and polymer physics principles that enable careful control over hydrogel stiffness and stress relaxation rate without impacting erosion rate, leading to hydrogel formulations with different combinations of stiffness and relaxation behavior, and allowing us to independently investigate the impact of each mechanical property in tissue modeling.

To demonstrate the potential use of these materials for in vitro tissue modeling, we explore how viscoelastic network properties impact the morphology of human neural progenitor cells (NPCs) over 7 days of culture.

Given the location of endogenous NPCs in the dentate gyrus of the brain, in vitro models are critical to further study of human brain development and disease progression [43, 44].

2 | Results and Discussion

2.1 | Tuning Stress Relaxation Through Reaction Kinetics

The hydrogels used in this work are comprised of recombinant HA and ELP, termed HELP hydrogels, with the total polymer weight percentage being kept constant at 2 wt.% (1 wt.% HA and 1 wt.% ELP) in all formulations. We chose a recombinant ELP variant that incorporates the fibronectin-derived RGD amino acid sequence that provides cell-adhesive interactions (Figure 1A) [31, 32, 34]. To enable dynamic crosslinking, the ELP is chemically modified with hydrazine (HYD) moieties, as described in our previous work [28, 32]. Similarly, HA was functionalized with either aldehyde (ALD) (Figure 1B) or benzaldehyde (BZA) (Figure 1C), to form dynamic hydrazone bonds with the HYD displayed by ELP (Figure 1D). The reaction kinetics for ALD-HYD are known to be faster than those for BZA-HYD, resulting in different rates of dynamic bond formation and dissociation [42, 45]. To evaluate the effect of reaction kinetics on bulk hydrogel stiffness, we used three hydrogel formulations with different ratios of HA-ALD and HA-BZA (0:100, 50:50, 100:0), while keeping the HA M_w constant (60 kDa). For HELP gels formulated with 6% functionalized HA, there were no statistically significant differences in the plateau storage modulus (G') among the three ALD:BZA ratios (0:100, 50:50, and 100:0), with G' values of 268.9 ± 48.5, 356.7 ± 18.3, and 235.3 ± 10.5 Pa, respectively, (mean ± standard deviation), suggesting that G' is independent of the ALD:BZA ratio (Figure 1E). We then formulated a family of stiffer gels by increasing the HA functionalization to 12%. As before, we observed that the ALD:BZA ratio had a small but non-significant impact on final gel stiffness, with G' values of 770.5 ± 58.8, 714.9 ± 104.9, and 630.1 ± 79.0 Pa, for 0:100, 50:50, and 100:0 ALD:BZA ratios, respectively (mean ± standard deviation) [29].

In contrast, the stress relaxation kinetics were found to strongly depend on the bond kinetics (Figure 1F). The higher the ALD:BZA ratio, the faster the stress relaxation kinetics, with HA-ALD (100:0) gels dissipating 50% of the applied stress after about 2000 and 4000 s, for 6% and 12% functionalization, respectively. In contrast, when only BZA-functionalized HA is used (0:100), the relaxation kinetics are considerably slower; even after 12 h, the 12% functionalized HA HELP gel had only dissipated about 20% of the applied stress.

As expected, the differences in ALD:BZA reaction kinetics not only affected the time-scale of stress relaxation, but also the rate of passive hydrogel erosion (Figure 1G). HELP hydrogels comprising only HA-ALD (100:0, 12% functionalization) erode considerably over a period of three days (25%) and almost completely after 14 days, while gels consisting of only HA-BZA (0:100, 12% function-

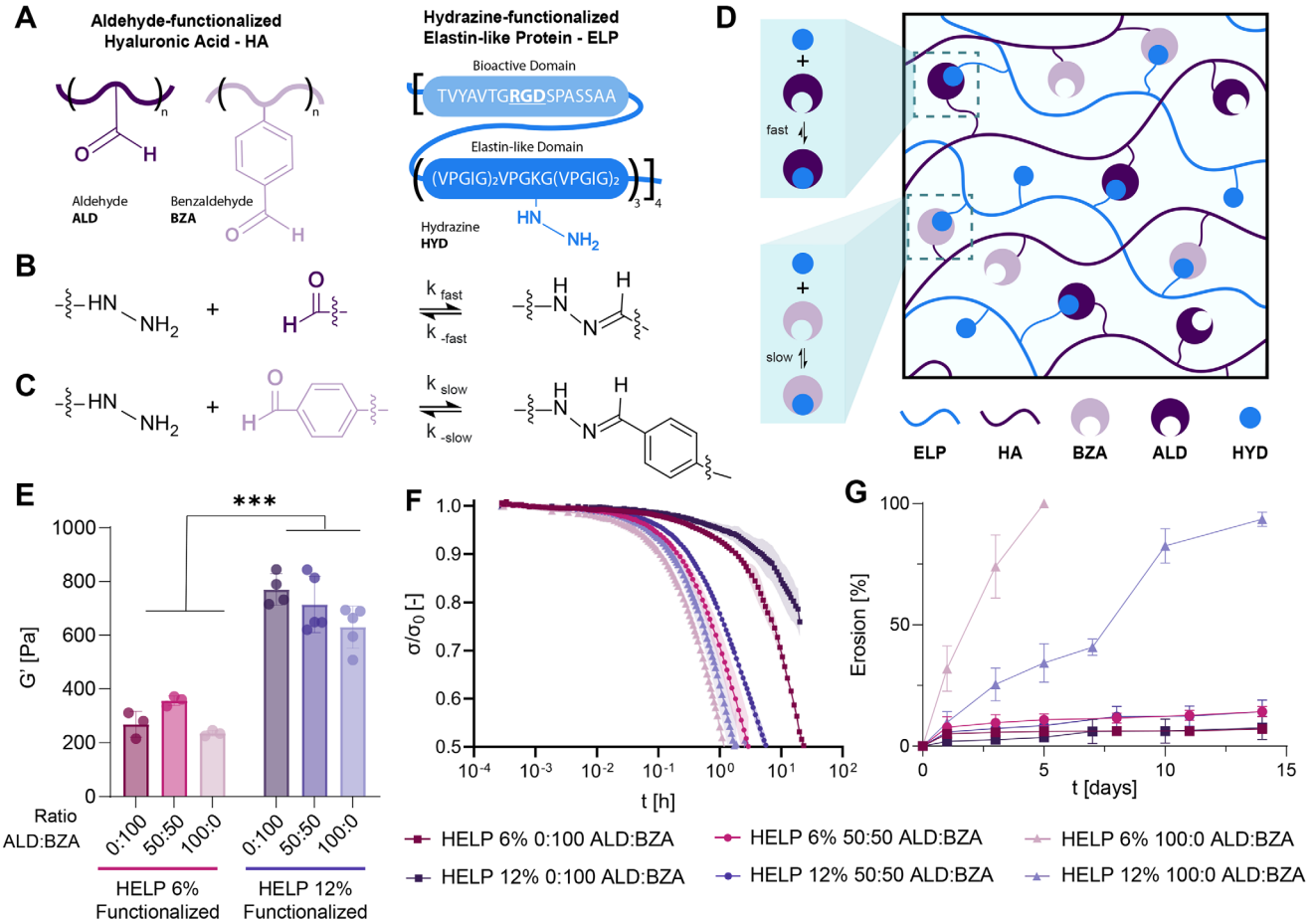

FIGURE 1 | Reaction kinetics control stress relaxation kinetics and erosion profile. (A) Schematic of hyaluronic acid (HA) functionalized with aldehyde (ALD) or benzaldehyde (BZA), and the elastin-like protein (ELP), including amino acid sequence, functionalized with hydrazine (HYD). (B,C) Representation of ELP-HYD and HA-ALD (B) and HA-BZA (C) forming a dynamic hydrazone bond with fast and slow reaction kinetics, respectively. (D) Schematic of a hydrogel network formed upon mixing HA-ALD and HA-BZA with ELP-HYD, termed HELP gel. (E,F). Storage modulus (G') at an angular frequency of 1 rad s^{-1} (E) and stress relaxation kinetics (F) of HELP hydrogels with different ratios of HA-ALD:HA-BZA, consisting of HA with a M_w of 60 kDa and a total amount of functionalization of either 12% (purple) or 6% (pink). (G) Erosion profile of HELP gels consisting of 60 kDa HA and with a total functionalization of 6% and 12% with either ALD (triangles) or BZA (squares). (E) One-way ANOVA, $p < 0.05$ *, $p < 0.01$ **, $p < 0.001$ ***, $p < 0.0001$ ****. Specific p-values are listed in Table S1.

alization) retain about 90% of their initial mass over the same time-frame. For HELP gels with the lower 6% functionalization, the erosion rate was even more rapid. Similar rapid erosion rates have been reported for other DCC-crosslinked hydrogels [27, 40, 46, 47]. This rapid erosion hinders the utility of these materials as scaffolds for in vitro tissue models. While the 50:50 formulation presents faster stress relaxation and good stability, it requires the synthesis and characterization of three different biopolymers: ELP-HYD, HA-ALD, and HA-BZA. Thus, while tuning of the crosslinker reaction kinetics is a straightforward way to achieve faster stress-relaxing hydrogels, these materials have practical limitations due to the interplay between synthesis demands, stress relaxation limits, and erosion kinetics. Given these results, we aimed at decreasing the synthesis burden by exploring the impact of other molecular parameters on the hydrogel viscoelastic properties. Specifically, we vary the HA molecular weight and the crosslinking density to formulate a two-component biopolymer system, rather than a three-component system, with tunable stress relaxation and stiffness, while maintaining high stability.

2.2 | Impact of Molecular Weight on Stiffness and Stress Relaxation Kinetics

As an alternative to the use of crosslinking reaction kinetics to control HELP gel stress relaxation rate, we next explored how HA M_w could alter HELP gel mechanics while keeping the ALD:BZA ratio and degree of functionalization constant (0:100 and 12%, respectively) (Figure 2A). We observed that the HA M_w did have an appreciable impact on both hydrogel stress relaxation rate (Figure 2B) and stiffness (Figure 2C). Consistent with previous results, increasing the M_w results in an increase in hydrogel stiffness (G') due to an increase in polymer entanglements (Figure 2C) [28, 48].

Interestingly, an inverse parabolic relationship was observed when evaluating the effect of HA M_w on network stress relaxation kinetics (Figure 2D,E). Increasing HA M_w from 20 to 60 kDa resulted in slower stress relaxation kinetics (Figure 2B,D,E). This decrease is expected when the relaxation time (τ) is governed

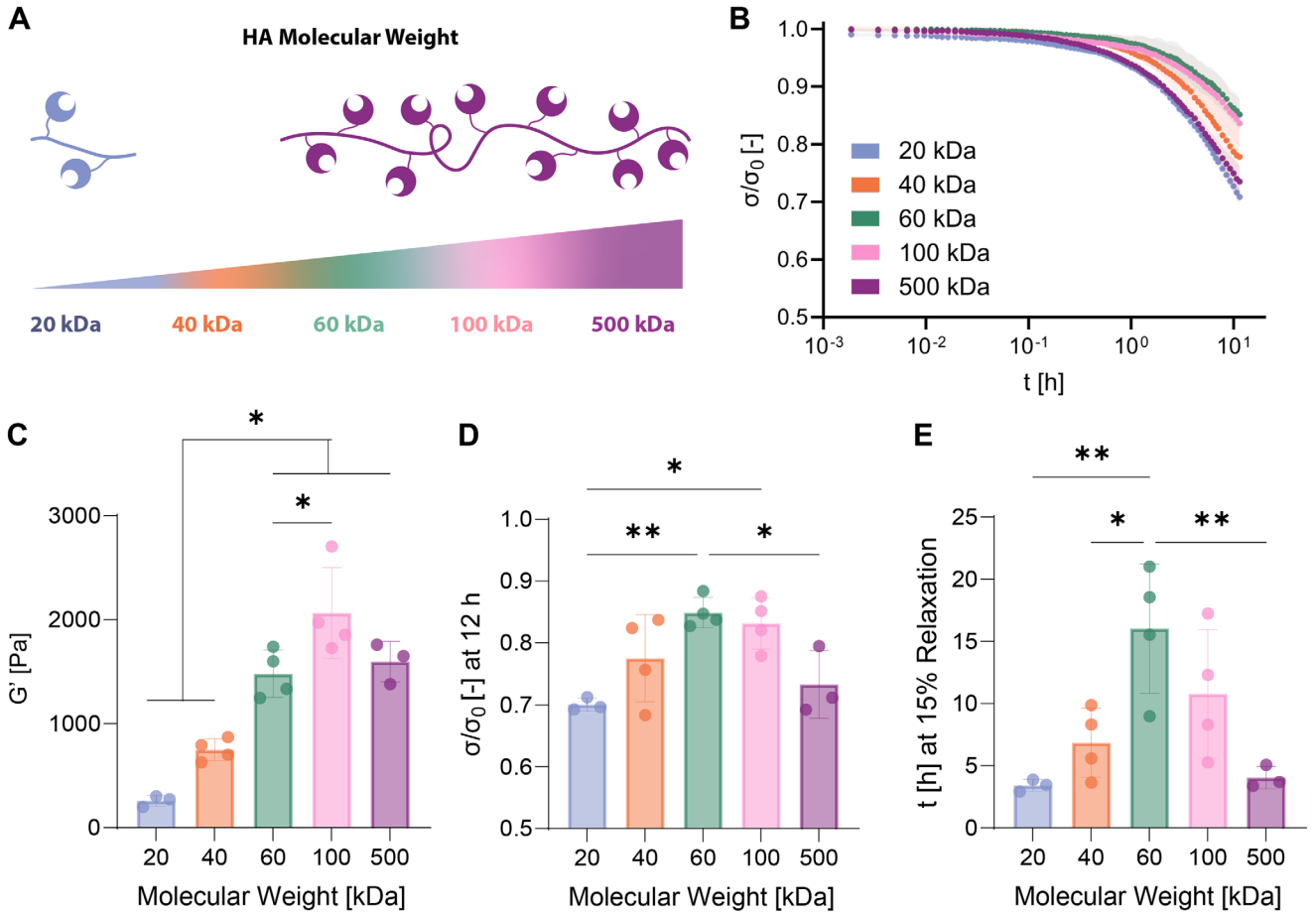

FIGURE 2 | Stiffness and stress relaxation kinetics of HELP hydrogels are tuned through HA M_w. (A) Schematic and color code of the different HA M_w formulations used in the study. All formulations used HA-BZA 12% functionalized, Figure S1. (B) Fraction of non-dissipated stress (σ/σ_0) against time. (C) Storage modulus (G') at an angular frequency of 1 rad s^{-1}. (D) Fraction of non-dissipated stress after 12 h. (E) Time necessary to dissipate 15% of applied stress. (C–E) One-way ANOVA, $p < 0.05$ *, $p < 0.01$ **, $p < 0.001$ ***, $p < 0.0001$ ****. Specific p-values are listed in Table S2 (C), Table S3 (D), and Table S4 (E). (B–E) Averages of $n \geq 3$ with standard deviation.

by entanglements between neighboring polymers, similar to that observed for physical networks and polymer melts, where relaxation time scales as $\tau \sim M_w^z$, where z is a scaling factor [49–51]. However, as HA M_w was further increased to 100 kDa and higher, the stress relaxation kinetics began to speed up again. This phenomenon is highlighted by observing that the stress relaxation profiles of the 20 and 500-kDa HELP gels are similar (Figure 2B) despite the 500-kDa HELP gel being 7.5-fold stiffer (Figure 2C). This trend suggests that the stress relaxation behavior of DCC-crosslinked hydrogels cannot be accurately predicted by simply applying traditional polymer physics models for entangled polymer melts.

2.3 | Modified Maxwell Modeling of DCC Hydrogels

Given this divergence from the expected stress relaxation behavior based on polymer melt modeling, we hypothesized that the mismatched sizes of the polymer chains, i.e. longer HA (> 100 kDa) and relatively short ELP (≈ 40 kDa), could be impacting the observed mechanics. Previously, higher polymer M_w has been shown to cause network defects and possible entanglements in the HELP system, which can affect other properties such as erosion profile, stiffness, and injectability [28]. For example, while polymer M_w does not typically impact hydrogel stiffness for irreversibly crosslinked networks, the brachiation theory of reversibly crosslinked polymer networks predicts that as polymer M_w increases, the hydrogel stiffness also increases due to a greater number of possible percolating connections throughout the gel [48].

By extension, here we propose that the mismatch in chain sizes (i.e., a large difference in relative polymer size) can lead to different polymer reptation [52] and diffusion regimes that affect the final relaxation profile to a greater extent than the kinetics of the DCC bonds. To explore this idea in an empirical model, we introduce the parameter q, which is the ratio of HA to ELP molecular weight. When the HA chain is smaller than the ELP polymer (i.e., HA ≈ 20 kDa, ELP ≈ 40 kDa, $q = 0.5$), the HA chains are unable to span across multiple neighboring ELP chains, [28, 53] leading to shorter or no percolating paths, increasing chain mobility, and allowing for faster relaxation (Figure 3A). At matched sizes of HA and ELP polymers (i.e. HA ≈ 40 kDa, $q = 1.0$), we envision an ideal network with continuous percolating connections and optimal crosslinking at

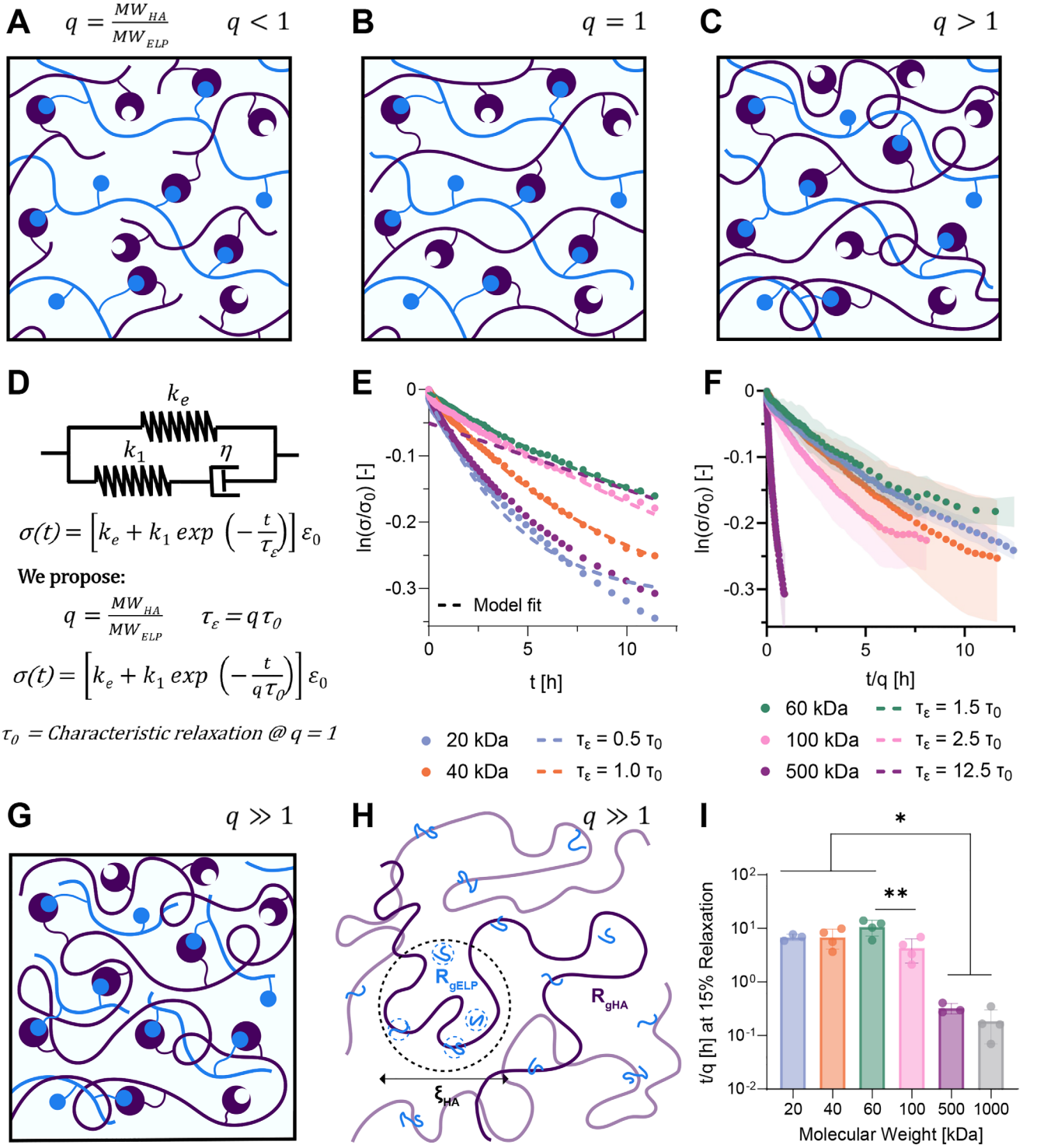

FIGURE 3 | Theoretical framework for the viscoelastic behavior of DCC gels with mismatched M_w (A–C) Schematic of polymer networks formed when mixing ELP-HYD (blue) with HA-BZA (purple) of different M_w, where $q = M_{wHA}/M_{wELP}$. (A) When $q < 1$, short percolation paths are formed. (B) When $q = 1$, a more uniform continuous network is formed. (C) When $q > 1$, a continuous and entangled network forms. (D) Modified Maxwell Model of viscoelasticity including q parameter to account for polymer mismatched sizes. (E) Natural log of fraction of non-dissipated stress (σ/σ_0) against time for all formulations (average of n = 3-4), compared to the theoretical fit of Modified Maxwell Model. Fitted values for Modified Maxwell Model are listed in Table S5. (F) Natural log of fraction of non-dissipated stress (σ/σ_0) against time normalized with respect to the q parameter for all formulations (average of n = 3–4). (G) Schematic of polymer networks formed where $q >> 1$, leading to the trapping of the shorter ELP chains within defects and entanglements, preventing them from making effective percolating paths. (H) Schematic of HELP gel with large q value, the large HA chains (purple, $R_{g_{HA}}$) are in a semi-dilute regime with short ELP chains (blue, $R_{g_{ELP}}$) in the dilute regime, such that many ELPs fit within one HA correlation length (ξ_{HA}). (I) Time necessary to dissipate 15% of applied stress for the different HA M_w HELP formulations normalized with respect to q parameter. One-way ANOVA, $p < 0.05$ *, $p < 0.01$ **, $p < 0.001$ ***, $p < 0.0001$ ****. Specific p-values are listed in Table S6.

the stoichiometric ratio of the hydrazone bond (Figure 3B) [28]. When the HA polymer is slightly larger than the ELP polymer (i.e. HA ≈ 60–100 kDa, $q = 1.5 - 2.5$), the HA would not only span across neighboring ELP chains and create long percolating paths, but also loop and entangle around the ELP chains, [28] thus decreasing chain mobility (Figure 3C).

To investigate this hypothesis, we propose applying a modified version of the phenomenological Maxwell standard linear solid model commonly used for viscoelastic materials [54–56]. In this Modified Maxwell model, the elastic behavior is represented by a spring with constant k_e, while the viscous part of the material is modeled through a dashpot with viscosity η, coupled to a spring with constant k_1, such that the characteristic relaxation time is defined as $\tau_\epsilon = \eta/k_1$ (Figure 3D). In this model, stress relaxation behavior after an applied constant strain is mathematically represented by:

$$\sigma(t) = [k_e + k_1 exp(-\frac{t}{\tau_\epsilon})] \cdot \varepsilon_0 \quad (1)$$

Given the expected impact of relative sizes of larger polymers on diffusion rates and reptation, we propose to rescale the characteristic relaxation time with the molecular weight ratio q. This direct rescaling is also supported by the definition of the SLS Maxwel model, where $\tau_\epsilon \propto \eta$. Increasing polymer size typically results in increased polymer viscosity [57], directly increasing the damping effect represented by the η value. Here, we propose the inclusion of the parameter $q = \frac{M_{wHA}}{M_{wELP}}$ to account for the mismatched sizes of the polymer chains, such that the characteristic relaxation time is $\tau_\epsilon = q \cdot \tau_0$, and at $q = 1$, $\tau_\epsilon = \tau_0$ leading to:

$$\sigma(t) = [k_e + k_1 exp(-\frac{t}{q \cdot \tau_0})] \cdot \varepsilon_0 \quad (2)$$

When applying this empirical model to the stress relaxation profiles of our HELP hydrogels, we see that the model achieves good correlation with the experimental data for formulations with HA M_w spanning 20–100 kDa, with $R^2 > 0.98$ (Figure 3E, fitting values in Table S5). This modified model describes the behavior of the relaxation for all formulations with an HA M_w lower than 500 kDa, supporting our hypothesis that the different relaxation profiles are being driven by the mismatched sizes of the polymer chains, whose fitting values can be found in Table S5. Further, when scaling the relaxation behavior with respect to q, effectively normalizing and removing the impact of the mismatched polymer sizes, all the different formulations with $M_{wHA} \leq 100$ kDa collapse into the same relaxation profile (Figure 3F), despite having significantly different stiffness (Figure 2C). This suggests that formulations that fit this model have similar physical processes underlying their relaxation behavior, likely the kinetics of the DCC bonds, and that the differences are arising due to the mismatched polymer sizes. In addition, as each formulation has the same theoretical number of DCC crosslinks (given the constant functionalization of 12% BZA independent of HA M_w), this also implies that the changes in stiffness are likely driven by the mismatched polymer sizes.

However, this modified Maxwell model does not accurately predict the behavior of the higher molecular weight formulation (i.e., HA ≈ 500 kDa, $q = 12.5$). We hypothesize that the highly mismatched sizes of the two polymers lead not only to a mildly decreased chain mobility, but to the actual trapping of the shorter ELP chains within defects and entanglements, preventing them from making effective percolating paths (Figure 3G,H) [52, 58–61].

2.4 | Blob Theory Clarifies Mismatched Behavior

In an attempt to better understand the impact of this size mismatch, we propose to further refine the scaling laws describing solutions with polymers of mismatched sizes, similar to the system described here. To further highlight the increased probability to form entanglements as HA M_w increases, we can estimate the theoretical polymer fractions, Φ, for the two polymers in a good solvent and investigate their overlap regimes [57, 60, 62–64], as follows:

$$\Phi_i = \frac{\upsilon_p N_i n_i}{V_{total}} = \upsilon_p N_i c_i \quad (3)$$

where υ_p is the volume occupied by one Kuhn segment, N_i is the number of Kuhn segments of a chain of polymer i, and $\frac{n_i}{V_{total}} = c_i$ is the concentration of chains, n_i, per total volume. In this analysis, as we are considering the situation right *before* the chains start overlapping, we assume that the radius of gyration (R_g) is independent of the polymer fraction and that all chains are behaving as an unperturbed real-chain self-avoiding random walk in a good solvent in the dilute regime, such that $R_g \sim b\, N^{3/5}$, where b is the Kuhn length of each monomer [57, 60, 62]. Thus, the total volume is the sum of the volume occupied by the total amount of HA and ELP chains as follows:

$$V_{total} \sim n_{ELP} (bN_{ELP}^{3/5})^3 + n_{HA} (bN_{HA}^{3/5})^3 \quad (4)$$

At the overlap condition, the average volume of polymer chains equals the total volume, transitioning into the semi-dilute regime. Thus, assuming $\upsilon_p \sim b^3$, two independent overlap concentrations are determined:

$$1 \sim \frac{n_{ELP} (bN_{ELP}^{3/5})^3}{V_{total}} + \frac{n_{HA} (bN_{HA}^{3/5})^3}{V_{total}} \quad (5)$$

$$1 \sim \Phi_{ELP}^* N_{ELP}^{4/5} + \Phi_{HA}^* N_{HA}^{4/5} \quad (6)$$

$$\Phi_{ELP}^* \sim N_{ELP}^{-4/5} \quad : . \quad \Phi_{HA}^* \sim N_{HA}^{-4/5} \quad (7)$$

As we have a mixture of asymmetric polymers, it is important to remember that the weight concentration, C_i, in wt.% of both polymers is kept constant and equal in all our gel conditions (e.g., $C_{HA} = C_{ELP} = 1\ wt\%$). Thus, the number of chains, n_i, in the gel decreases with an increase in the molecular weight of the larger polymer chain. If we assume the molecular weight of the monomer for each polymer is the same, it follows that:

$$C_i = \frac{M_i}{V_{total}} = \frac{n_i MW_i}{V_{total}} = c_i MW_i \quad (8)$$

$$c_{HA}\,M_{wHA} = c_{ELP}\,M_{wELP} \;\;\therefore\;\; \frac{c_{ELP}}{c_{HA}} = \frac{n_{ELP}}{n_{HA}} = \frac{M_{wHA}}{M_{wELP}} = q = \frac{N_{HA}}{N_{ELP}} \tag{9}$$

It follows that the q parameter has an impact on the overlap concentration of HA:

$$\Phi^*_{HA} \sim q^{-4/5} N^{-4/5}_{ELP} \tag{10}$$

Thus, by changing the ratio of asymmetry, q, while keeping all polymer weight concentrations constant, it allows us to move between different semi-dilute regimes ($\Phi_i >> \Phi^*_i$), leading to highly entangled solutions and additional relaxation modes. Particularly, three cases could be considered: (A) a dilute large polymer (HA) within a semi-dilute matrix of short polymer (ELP), (B) a dilute short polymer within a semi-dilute matrix of large polymer, and (C) both polymers are in the semi-dilute regime. The analysis of these different cases is presented in the Methods S1.

The inverse relationship of $\Phi^*_{HA} \sim q^{-4/5}$ suggest the overlap concentration of the HA will be smaller than Φ^*_{ELP}, indicating that the 500 KDa-HA HELP formulation is likely in the second scenario: a dilute short polymer (ELP) within a semi-dilute matrix of long polymer (HA). When discussing polymer solutions, the concept of 'blob' and correlation length becomes important, which can be defined as the region of a polymer chain of size ξ that does not interact with other chains, but still presents an excluded volume [57, 60, 62, 65]. At length scales larger than the 'blob' size, the Flory theorem suggests we can consider that a chain behaves as an ideal chain of blobs [63], such that R_g relates to the number of monomers, N, as follows:

$$R_{g_i} \sim \xi \left(\frac{N_i}{g}\right)^{1/2} \tag{11}$$

Here, g is the number of monomers per blob. To consider the excluded volume interactions within each 'blob', we can relate the correlation length, ξ, to g by considering the blob as a swollen coil in a good solvent ($\nu = 3/5$) [60, 62], such that:

$$\xi \sim b\, g^{3/5} \tag{12}$$

Further, in the semi-dilute regime of a polymer i, the correlation length has been related to the polymer fraction Φ [60, 62, 65]:

$$\xi_i \sim b\, \Phi_i^{-3/4} \tag{13}$$

Thus, for the long polymer, HA, in this semi-dilute regime, R_g would be as follows:

$$R_{g_{HA}} \sim \xi \left(\frac{N_{HA}}{g}\right)^{1/2} \sim b\, \Phi^{-3/4}_{HA} \left(\frac{N_{HA}}{\Phi^{-5/4}_{HA}}\right) \tag{14}$$

$$R_{g_{HA}} \sim b\, \Phi^{-1/8}_{HA}\, N^{1/2}_{HA} \tag{15}$$

As in our analysis, we have defined $q = N_{HA}/N_{ELP}$.

$$R_{g_{HA}} \sim b\, \Phi^{-1/8}_{HA}\, q^{1/2}\, N^{1/2}_{ELP} \tag{16}$$

For the short polymer in our system, ELP, R_g will depend on whether the ELP chain is unperturbed within the HA 'blob' or if it extends beyond the 'blob'. Here, we can analyze the ratio α of the correlation length to the unperturbed polymer size of the ELP (Methods S1):

$$\alpha \sim \frac{\xi}{b\, N^{3/5}_{ELP}} \sim \left(\frac{\Phi^*_{ELP}}{\Phi_{HA}}\right)^{3/4} \tag{17}$$

Assuming that the system is exactly at the overlap condition, the start of the semi-dilute HA regime, such that $\Phi_{HA} = \Phi^*_{HA}$. It follows, that:

$$\alpha \sim \left(\frac{\Phi^*_{ELP}}{\Phi^*_{HA}}\right)^{3/4} \sim \left(\frac{N^{-4/5}_{ELP}}{N^{-4/5}_{HA}}\right)^{3/4} \sim\; q^{3/5} \tag{18}$$

Thus, as the mismatch sizes q increases, the more likely the ELP chain would be to be unperturbed within the HA blob, and the radius of gyration would be $R_{g_{ELP}} \sim b\, N^{3/5}_{ELP}$, Figure 3H. As α decreases, the ELP chain will extend beyond the HA correlation length (Methods S1). This analysis of R_g of the two polymer components allows the comparison of their relative volume, V, in a polymer solution with respect to the q value:

$$\frac{V_{HA}}{V_{ELP}} \sim \frac{R^3_{g_{HA}}}{R^3_{g_{ELP}}} \propto q^{3/2} \tag{19}$$

Thus, as the HA M_w becomes much larger (q increases), the volume of the HA chain is exponentially higher than that of the ELP. For instance at $q = 12.5$, for the 500 kDa HA, the volume occupied by the HA chain is roughly ~ 45 times larger than that of the ELP, Figure 3H. Therefore, the analysis through this two-component blob theory clarifies our experimental results. This size mismatch could potentially prevent the smaller ELP chains from forming crosslinking bonds across multiple polymer chains and inhibit the creation of a percolated network. In this scenario, we reasoned that a new relaxation mode would dominate, driven by the entanglements and interactions of the larger chain rather than the kinetics of the DCC bonds (Figure 3G,H).

To test this hypothesis, we designed a formulation with an even larger HA M_w (i.e., HA $\approx$ 1 MDa, $q = 25$), still functionalized with BZA at 12%. We estimate the relative size of the 1 MDa HA to be about 125-fold larger than that of the ELP polymer. Interestingly, the 1 MDa formulation also relaxes very rapidly, similar to the rate of the 500 kDa formulation, but displays a more linear temporal relaxation, suggesting that the relaxation behavior is primarily governed by entanglements from the onset of relaxation. This is further supported by analyzing the normalized relaxation time (t/q) to reach 15% relaxation, which is the same order of magnitude for all formulations with HA $M_w \leq 100$ kDa, and drops to a significantly lower value for formulations with HA $M_w \geq 500$ kDa (Figure 3I). Thus, as an alternative strategy to selecting different DCC crosslinking reactions to control the hydrogel stress relaxation rate, we demonstrate that tuning q by altering the M_w of one of the polymer components can significantly impact network relaxation dynamics.

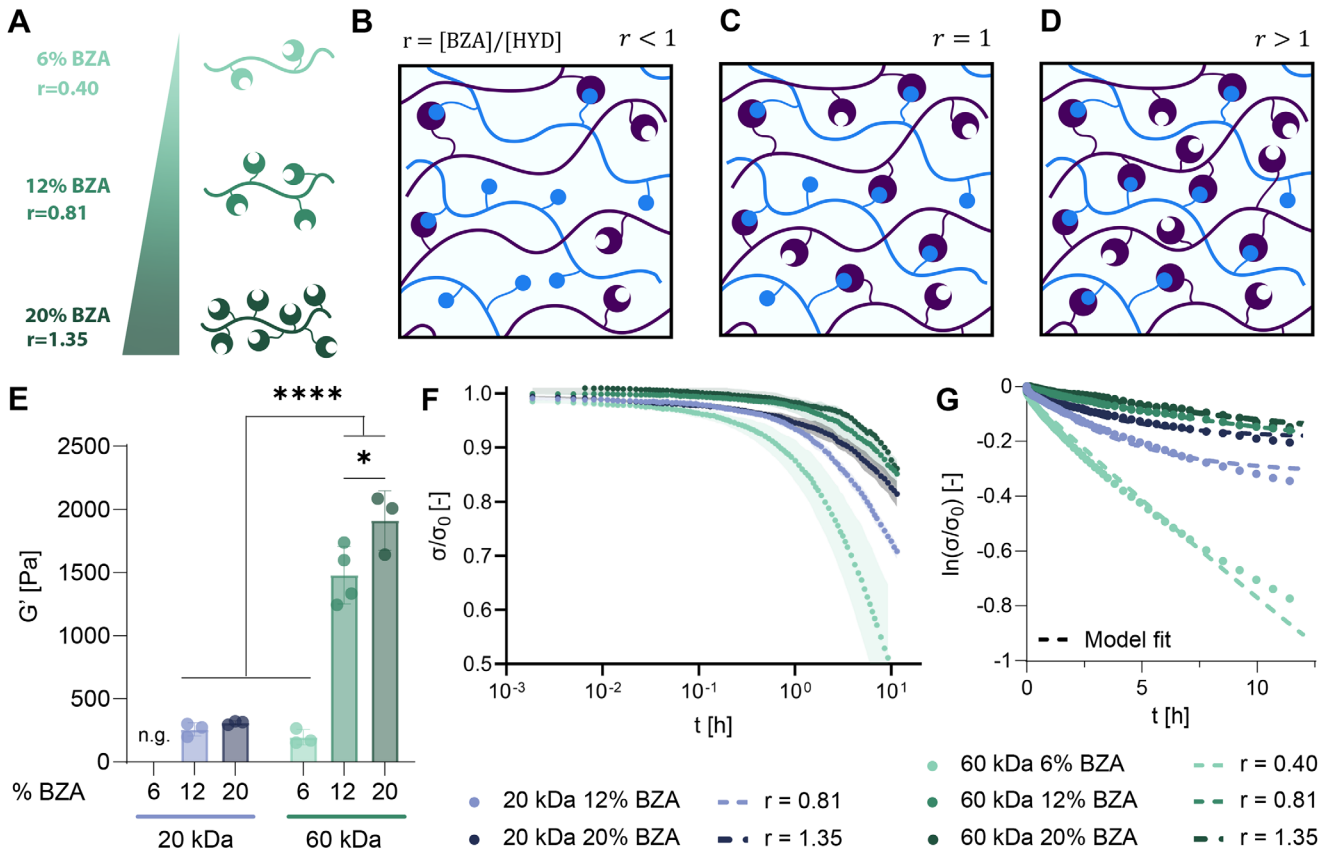

FIGURE 4 | The stiffness and stress relaxation of HELP gels is tuned through the degree of functionalization of HA. (A) Schematic and color code of the different HA degrees of functionalization (Figure S1) used in the study, resulting in different ratios of the DCC reactive groups ($r = [BZA]/[HYD]$). (B–D) Idealized schematics of polymer networks formed when mixing ELP-HYD (blue) with HA-BZA (purple) with different degrees of functionalization, resulting in $r < 1$ (B), $r = 1$ (C), and $r > 1$ (D). (E) Storage modulus, G', for the different HELP formulations. One-way ANOVA, $p<0.05$ *, $p<0.0001$ ****. Specific p-values are listed in Table S7. (F) Fraction of non-dissipated stress (σ/σ_0) against time. (G) Natural log of fraction of non-dissipated stress (σ/σ_0) against time for formulations compared to the theoretical fit of Modified Maxwell Model. Fitted values for Modified Maxwell Model are listed in Table S5. (E–G) Averages of $n \geq 3$ with standard deviation.

2.5 | Impact of HA Degree of Functionalization on Stiffness and Stress Relaxation Kinetics

Having explored the impact of M_w mismatch on stress relaxation, we next set out to investigate the effect of the degree of chemical functionalization of HA. To aid in our analysis, we define r as the stoichiometric ratio between BZA and HYD crosslinking groups. We first tested functionalization at 6%, 12%, and 20% BZA for the 20-kDa and 60-kDa HA M_w formulations, corresponding to stoichiometric ratios (r) of BZA:HYD reactive groups of 0.41, 0.81, and 1.35, respectively, (Figure 4A–D). Here, it is important to highlight that at $r = 1$, the concentration of available reactive groups will match the stoichiometry of the hydrazone bond reaction, which would be expected to produce the stiffest hydrogel in a traditional, static covalent crosslinked system (Figure 4C). However, for DCC chemistry, the reversible crosslinking reaction has an equilibrium constant (K_{eq}), which controls the number of on- and off- bonds and is governed by Le Châtelier's principle [45]. Thus, by increasing the concentration of BZA ($r > 1$), we favor the formation of new bonds, increasing the amount of crosslinks formed at any given time within the network (Figure 4D). In general, this is supported by our data, where the increased functionalization of HA leads to increased stiffness within the same family of HA M_w hydrogels, attributed to a higher crosslinking density (Figure 4E). In contrast, when $r < 1$, the low amount of crosslinks leads to lower stiffness. This is particularly evident in the 20-kDa HA functionalized with 6% BZA, where no hydrogel is formed, likely due to the combined effect of low functionalization and short HA chains leading to the absence of a percolating network (Figure 4B,E). Thus, the degree of functionalization is an experimental variable that can be used to alter the network connectivity, and hence stiffness, in DCC-crosslinked hydrogels.

We reasoned that these alterations in network connectivity would also offer a means to tune the stress relaxation rate. Consistent with this idea, at both lower and intermediate HA M_w (*i.e.*, 20 and 60 kDa), the hydrogels exhibited changes in stress relaxation rate. Higher crosslinking density led to decreased chain mobility, with fewer degrees of freedom and slower relaxation, as previously reported in literature (Figure 4F,G). This behavior is observed at low HA M_w, with the 12% BZA formulation relaxing faster than the 20% BZA, as well as at intermediate HA M_w, with the 12% BZA formulation relaxing significantly slower than its 6% counterpart. Interestingly, there seems to be a plateau to the contribution of crosslinking density in slowing down relaxation, as the 60-kDa HELP gels with 12% and 20% BZA functionalization have overlapping relaxation profiles. Importantly, our

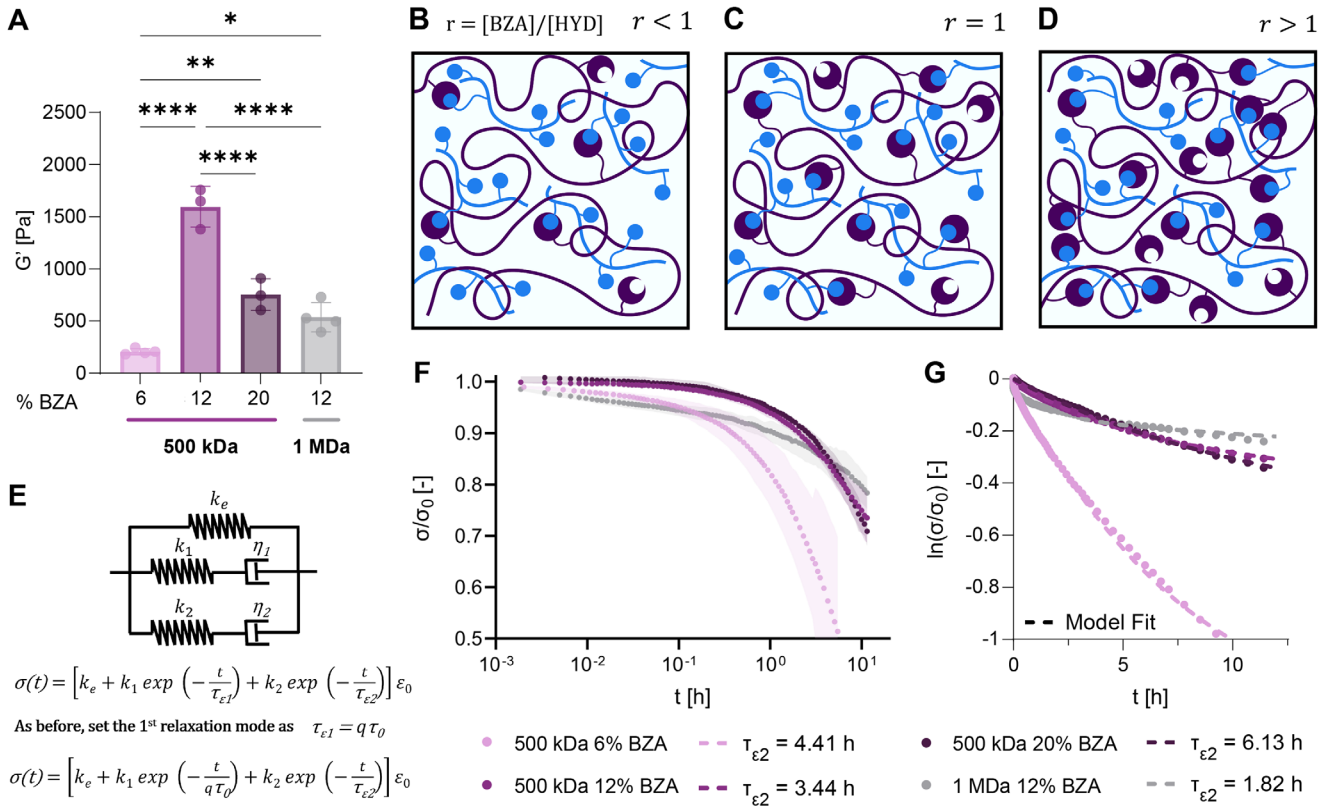

FIGURE 5 | Stress relaxation behavior in hydrogels with large polymer size mismatch is driven both by entanglements and DCC kinetics. (A) Storage modulus (G') for the different HELP formulations with high HA M_w. One-way ANOVA, $p<0.05$ *, $p<0.01$ **, $p<0.0001$ ****. Specific p-values are listed in Table S8. (B–D) Schematic of polymer networks formed when mixing ELP-HYD (blue) with HA-BZA (purple) with different % functionalization, where $r = [BZA]/[HYD]$, resulting in $r < 1$ (B), $r = 1$ (C), and $r > 1$ (D) (E) Two-Component DCC Network model of viscoelasticity, including both the q parameter to account for polymer mismatched sizes, and a second spring-dashpot representing the additional relaxation mode. (F) Fraction of non-dissipated stress (σ/σ_0) against time. (G) Natural log of fraction of non-dissipated stress (σ/σ_0) against time compared to the theoretical fit of Two-Component DCC Network model. Fitted values for Two-Component DCC Network model are listed in Table S9. Averages of $n \geq 3$ with standard deviation.

modified Maxwell model accurately describes the stress relaxation behavior for these five HELP formulations (Figure 4G), with the decrease in crosslinking density captured by a decrease in the k_e (Table S5 and Figure S2) value for hydrogels with lower degree of functionalization. Thus, while keeping the identity of the DCC chemistry the same (i.e., all BZA-HYD crosslinks), the stress relaxation rate of the hydrogel can be tuned either by changing polymer molecular weight or by changing the degree of functionalization.

2.6 | Modified Maxwell Model for Large Polymer Chains

Interestingly, for HELP gels with relatively high HA M_w ($\geq$ 500 kDa) where there is a large HA:ELP M_w mismatch ($q >> 1$), the degree of HA functionalization impacts gel mechanics in a different way compared to formulations with q near 1. In particular, the stiffness decreases considerably as HA functionalization is increased from 12% to 20% (i.e., r from 0.81 to 1.35) (Figure 5A). This supports our hypothesis that the large M_w mismatch is leading to the formation of a network with more entanglements and defects that prevent effective crosslinking (Figure 5B–D) [52, 61, 66]. Consistent with this idea, as q is increased even further (HA $\approx$ 1 MDa, $q = 25$) while keeping the degree of functionalization constant (12%, $r = 0.81$), the resulting gel stiffness continues to decrease (Figure 5A).

The earlier discussion on the overlap concentrations and blob theory in the HELP system can further improve our understanding, as the larger q will lead to a transition into a semi-dilute regime leading the relative volumes occupied by each polymer to be exponentially different. Our earlier analysis suggests that as the 'q' increases, the smaller chains are unable to create a percolated network, and a novel relaxation mode dominates, driven by interactions of the larger polymer chain. Thus, this analysis supports the presence of a secondary mode of relaxation as a hypothesis consistent with our observed trends.

Another important parameter is the predicted entanglement concentration for the HA polymer, which similarly scales with $q^{-4/5}$ (Methods S2), suggesting the higher the mismatch, the lower the HA entanglement concentration. If we consider the entanglement concentration of solely unmodified HA in a good solvent, we can use literature data to estimate the entanglement concentration, $C^{entanglement}_{HA_{500kDa}} \approx 2.24$ $wt\%$ and $C^{entanglement}_{HA_{1MDa}} \approx 1.31$ $wt\%$ (Table S10), which is similar or lower than the concentration of the precursor HA-BZA solutions, 2 $wt\%$, suggesting the

precursor solutions are already partially entangled [28, 48, 51, 57, 58]. Thus, as the HA M_w increases, homogeneous mixing of the two polymeric solutions becomes more challenging, resulting in uneven network formation with possible defects. This can prevent the formation of a uniformly crosslinked network and lead to low effective crosslinking density and lower stiffness (Figure 5A). As with the intermediate HA M_w formulations, the higher amount of entanglements and decreased chain mobility for higher HA functionalization are also reflected in the observed stress relaxation behavior. Similar to formulations with intermediate HA M_w, lower functionalization leads to a higher stress relaxation rate that decreases with increasing functionalization up to a plateau value (Figure 5E).

To probe network topology and investigate the presence of entanglements, we performed large amplitude oscillatory rheology (LAOS) of our formulations [67, 68]. Literature suggests that the presence of a loss modulus overshoot in LAOS is indicative of entanglements that act as transient "solids" that are eventually forced to flow due to the ever growing external deformation [68]. Performing LAOS in our formulations with short (20-kDa) and large (1-MDa) HA M_w, we distinctly see the increase of strain overshoot indicative of the increase in local entanglements present in the formulations with large mismatched M_w, Figure S3. This evidence supports our blob theory-informed hypothesis that a secondary relaxation mode is present in highly mismatched HELP formulations.

However, as described earlier, the empirically based single-dashpot Maxwell model modified with q terms still does not accurately fit experimental data for very large q values (Figure 3E). Based on our empirical findings, we reasoned that this was likely due to the larger number of local entanglements present in the longer HA chains, which would also contribute a relaxation timescale to the overall network viscoelasticity. With the intention to provide an interpretation of the impact of mismatched molecular weight within the semi-dilute regime on relaxation behavior, we propose an additional modification to our model. Here, to capture this extra relaxation mode, we propose the addition of a second spring-dashpot to represent entanglement relaxation, with spring constant k_2 and viscosity η_2, such that the characteristic relaxation time is defined as $\tau_{\epsilon 2} = \eta_2/k_2$ (Figure 5E). In this Two-Polymer DCC Network model, the stress relaxation behavior after an applied constant strain is mathematically represented by:

$$\sigma(t) = [k_e + k_1 exp(-\frac{t}{q \cdot \tau_0}) + k_2 exp(-\frac{t}{\tau_{\epsilon 2}})] \cdot \varepsilon_0 \qquad (20)$$

With this further modification, the Two-Polymer DCC Network model accurately captures the viscoelastic behavior of all formulations tested, including the high q formulations (i.e. HA M_w 500 kDa and 1 MDa) (Figure 5G, Figures S2, S4, and Table S9).

To investigate the applicability of this model to other hydrogel formulations, we replaced our ELP-HYD with a 60-kDa HA-HYD, creating an HA-only, homopolymer formulation. This HA-HYD was mixed with 20-kDa, 60-kDa, 500-kDa, and 1-MDa HA-BZA, all modified at 12%, yielding a range of MW ratios: q = 0.33, 1, 8.33, and 16.66, respectively. Overall, formulations without the ELP relaxed more quickly (Figure S5). This is likely due to the formation of ELP aggregates at 37°C [28, 32, 69], which restricts the movement of the polymer chains, thus slowing down relaxation. In the HA-only system, we see the relaxation behavior of the 1-MDa formulation and the 500-kDa formulation overlap. This suggests that although the polymer size transition ratio is different from the HELP system, at large enough MW mismatches, the relaxation is influenced significantly by local entanglements. Both empirical models were applied to the HA-only system, and the Two-Polymer DCC Network model provided a better fit for the behavior of this system than the single-component modified SLS Maxwell (Tables S11, S12 and Figures S5, S6), supporting our hypothesis that mismatched MW sizes can lead to hydrogels with two relaxation modes.

Regarding the HELP system, this empirically-based phenomenological model suggests that at low functionalization, the relaxation is dominated by the movement of the long uncrosslinked but entangled chains, leading to a faster rate of relaxation (Figure 5B). By increasing the functionalization, the kinetics of the bonds slow down the relaxation (Figure 5C) as the crosslinking density increases. However, at high functionalization, there is a substantial decrease in crosslinking density as reflected by the decrease in stiffness. Thus, this suggests that the slower stress relaxation seen at high functionalization in high HA M_w formulations is likely also dominated by the movement of entangled chains, which have highly restricted mobility due to entrapment of the ELP chains (Figure 5D). This decrease in mobility is also captured by our model; while $\tau_{\epsilon 2}$ has similar values for our 6% and 12% BZA formulations of 500 kDa HA, it almost doubles for our 20% BZA formulation.

2.7 | Hydrogel Viscoelasticity Alters Neurite Morphology

After establishing these design rules for how molecular-level polymer parameters control the stiffness and stress relaxation kinetics of HELP hydrogels, we next evaluated the effect of gel mechanics on cellular behavior. Specifically, we explored how gel viscolasticity impacted the morphology and neurite outgrowth of human-induced pluripotent stem cell-derived neural progenitor cells (hiPSC-NPCs), as these cells are known to be mechanosensitive [21, 29, 30]. There are inherent difficulties associated with directly studying the human brain, as samples are restricted to post-mortem and biopsy tissues, providing limited information since they are constrained to a specific timepoint in neural development and disease progression [43, 44, 56]. In addition, the information acquired by functional neuroimaging is also limited due to inherent resolution challenges [70]. Moreover, the applicability of in vivo models developed from studying rodent brains to human physiology is restricted by the anatomical and physiological disparities between the two species (i.e., rodent and human) [71, 72]. Therefore, the advancement of human in vitro models are critically important to study human brain development and disease. To probe the mechanical versatility of our HELP gel formulations and their application in 3D in vitro tissue culture models, we encapsulated hiPSC-NPCs in HELP gels of five different formulations (Figure 6).

One of the key advantages of controlling viscoelasticity through our chosen molecular parameters, HA M_w and degree of

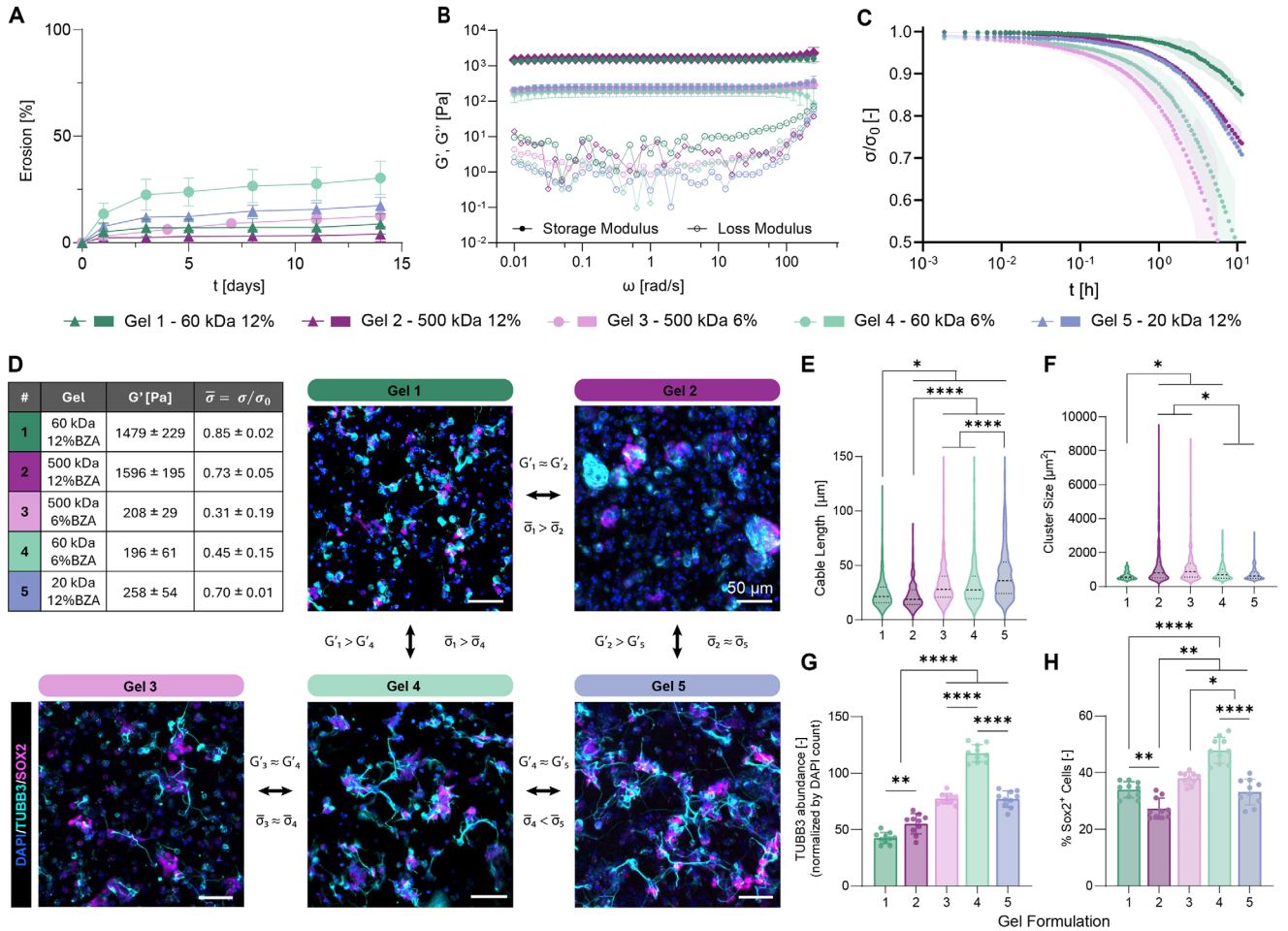

FIGURE 6 | The viscoelastic characteristics of hydrogels impacts neurite morphology in 3D tissue culture system. (A) Erosion profile of selected HELP gels. (B) Frequency sweep of selected HELP gel formulations ranging from 0.01 to 250 rad/s, storage modulus (G', filled symbols) and loss modulus (G'', open symbols). (C) Fraction of non-dissipated stress (σ/σ_0) against time. (D) Table with selected HELP gel formulations with their respective storage modulus (G'), and fraction of non-dissipated stress at 12 h ($\bar{\sigma} = \sigma/\sigma_0$), both reported as mean ± standard deviation, Top right. Representative maximum projection fluorescence images of hNPCs encapsulated at 30,000 cells μL^{-1} within all five gel formulations after 7 days of culture with labeled cell nuclei (DAPI, blue) and neuritic extensions (TUBB3, cyan), and stemness marker (Sox2, magenta), with comparison relationships. (E) Cable length of individual neurites through quantifying TUBB3-expressing projections with the SNT toolbox. (F) Cell-cluster sizes wuantified based on DAPI staining, identifying objects > 40 pixel units in diameter. Kruskal-Wallis, $p<0.05$ *, $p<0.0001$ ****. Specific p-values are listed on Table S13(E) and Table S14(F). (G). Tubulin abundance normalized by nuclei (DAPI) count. (H). Percentage of Sox2+ cells. One-way ANOVA, $p < 0.05$ *, $p < 0.01$ **, $p < 0.0001$ ****. Specific p-values are listed on Table S15(G) and Table S16(H). Images analyzed, N=10, with $n \geq 323$ (E) and $n \geq 116$ (F). Specific N and n values are listed in Table S17.

functionalization with BZA, is the increase in long-term hydrogel stability (Figure 6A). Standard approaches to tune stress relaxation by altering the DCC bond kinetics, such as incorporating ALD moieties as the crosslinking motif, have been shown to result in rapid hydrogel erosion (Figure 1G). Our unique approach retains the use of BZA moieties, known to have a slower on-off binding rate. This leads to a decrease in erosion for all selected gel formulations, with a maximum of 25% erosion over two weeks (Figure 6A), while ALD formulations experienced 75%–100% erosion over the same time period (Figure 1G). To allow for comparison between the relaxation behavior of all formulations analyzed in this paper, we present all relaxation profiles, characteristic times for 15% relaxation, and fraction of non-dissipated stress after 12 h in Supplementary Information (Figures S7 and S8). These data demonstrate that by tuning molecular parameters, we can achieve similar relaxation behavior as by altering DCC bond kinetics (Figure S7E). Having analyzed all potential formulations, we selected the HELP gel formulations such that we would have a set of stiffness-matched gels and a set of stress relaxation-matched gels (Figure 6B,C), allowing us to separately investigate the effects of each variable. The hydrogels selected for the in vitro study had the following HA M_w and degree of functionalization parameters: 60 kDa and 12% BZA (Gel 1), 500 kDa and 12% BZA (Gel 2), 500 kDa and 6% BZA (Gel 3), 60 kDa and 6% BZA (Gel 4), and 20 kDa and 12% BZA (Gel 5) (Figure 6D). Briefly, Gel 1 and Gel 2 have similar stiffness, while Gel 1 has a slower stress relaxation rate. 'Gel 2 and Gel 5 have a similar stress relaxation rate, but Gel 2 has a higher stiffness. Gel 1 has a higher stiffness and a slower stress relaxation rate than Gel 4. Gel 4 and Gel 5 have similar stiffness, but Gel 5 has a slower stress relaxation rate. Finally, Gel 3 and Gel 4 have similar stiffness and stress relaxation rate.

Encapsulated cells were exposed to identical media for 7 days and then immunostained for βIII-tubulin (TUBB3), a neuronal lineage marker and key component of neuritic projections, and Sox2, a marker of NPC stemness (Figure 6D) [29, 30]. Quantitative morphology metrics included measurements of cable length to compare neurite extension (Figure 6E) and cell cluster size to compare the propensity to form neurospheres (Figure 6F). NPCs frequently grow as neurospheres when cultured in suspension, and when encapsulated can grow either as neurospheres or dispersed cells [30]. In our earlier work, we have shown that hiPSC-NPCs encapsulated in fast stress-relaxing, intermediate stiffness ($G' \approx 800$ Pa) HELP gels using a 50:50 BZA:ALD ratio (12% functionalization) exhibited a highly branched morphology with neurites extending throughout the gel from dispersed cells [29].

When comparing Gel 1 and Gel 2 ($G'_1 \approx G'_2$ and $\overline{\sigma}_1 > \overline{\sigma}_2$), while the faster relaxation rate did not lead to increased neurite outgrowth, there was significantly higher expression of TUBB3 (Figure 6E–H). The expression of neural stemness marker Sox2 was higher in Gel 1, with a higher number of Sox2+ cells. There was also the presence of large cell clusters in Gel 2 (HA 500 kDa 12 %BZA formulation), which appeared to be where the majority of βIII-tubulin expression was localized. Looking at Gel 2 and Gel 5 ($G'_2 > G'_5$ and $\overline{\sigma}_2 \approx \overline{\sigma}_5$), these similar relaxation rates led to widely differing results, suggesting this phenomena may be driven by the lower stiffness of Gel 5, which resulted in increased neurite outgrowth, smaller cell clusters, and higher expression of both βIII-tubulin and Sox2. We saw similar behavior when comparing the cellular responses in Gel 1 and Gel 4 ($G'_1 > G'_4$ and $\overline{\sigma}_1 > \overline{\sigma}_4$), with the lower stiffness corresponding to longer neurites with higher expression of βIII-tubulin and Sox2. For Gel 4 and Gel 5 ($G'_4 \approx G'_5$ and $\overline{\sigma}_4 < \overline{\sigma}_5$), which are both of lower stiffness, the faster relaxation rate of Gel 4 corresponded to a higher expression of βIII-tubulin and Sox2, although the cable length, our metric for neurite outgrowth, was higher for Gel 5 (HA 20 kDa 12% BZA formulation), suggesting that there may be an optimal combination of stiffness and relaxation rate to promote neurite extension. An unexpected finding is that Gel 2, with intermediate relaxation rate ($\overline{\sigma}_1 > \overline{\sigma}_2 > \overline{\sigma}_4$) and high stiffness, presented the lowest cable length of all conditions. This formulation (Gel 2) also led to the formation of large cell clusters with high expression of βIII-tubulin (Figure 6F). These data may indicate that the higher HA M_w and the secondary relaxation mode driven by entanglements might hinder neurite outgrowth. One way to investigate this is to compare the formulations with similar stiffness and stress-relaxation rate, Gel 4 and Gel 3 ($G'_4 \approx G'_3$ and $\overline{\sigma}_4 \approx \overline{\sigma}_3$), but differing HA M_w (60 kDa and 500 kDa, respectively) (Figure 6F). Although they had similar cable lengths, the lower HA M_w formulation (Gel 4) resulted in higher expression of both βIII-tubulin and Sox2 and fewer cell clusters (Figure 6G,H). These data are consistent with the idea that higher HA M_w may impact cell morphology, potentially through secondary relaxation modes caused by polymer entanglements, leading to the formation of cell clusters. We hypothesize this behavior could be due to the lower crosslink concentration, which may lead to local relaxation rather than continuous bulk matrix relaxation. Previous work has shown that many cellular processes, including cell spreading and migration, have non-linear responses to matrix stiffness, stress dissipation, and the concentration of cell-receptor ligands [24, 29, 54, 73–76]. Our data suggest that neurite outgrowth is also a non-linear consequence of stiffness and stress relaxation rate. Specifically, we observe that the combination of high stiffness and fast stress relaxation rate prevents efficient neurite extension, while low stiffness and fast stress relaxation rate enhances neurite extension. Importantly, these non-linear interactions within biological systems highlight why it is technologically important to design materials with control over both stiffness and stress relaxation rate.

Overall, these results provide insight into the potential effects of both stiffness and stress-relaxation on cell morphology, agreeing with previous results and demonstrating that the synergy of lower stiffness with fast stress-relaxation rates can correlate with increased stemness maintenance and neurite outgrowth [21, 29, 30]. Further, the enhanced stability of these formulations lend themselves to future cellular biomechanics studies to explore in detail the mechanosignaling pathways responsible for the observed phenotypes.

3 | Conclusions

Three-dimensional models of in vitro tissue culture enable high-throughput drug screening, mechanistic studies, and the investigation of human development, making them indispensable for biomedical research. Further, their ability to recapitulate biochemical and mechanical characteristics of tissues allows the field to move away from animal studies and to explore in vitro models as animal-free "new approach methodologies" (i.e., NAMs). The use of hydrogels as 3D tissue culture models has been widely explored, as their tunable viscoelastic and biochemical properties are known to impact cell morphology and function. Particularly, DCC crosslinked gels have risen to prominence since the reversible nature of their bonds allows for the introduction of stress-relaxation, a key mechanical characteristic of native ECM. Traditional methods to tune the stress-relaxation and viscoelasticity of DCC gels are based on bond kinetics, which directly affect gel erosion rates, typically preventing their use for multi-day 3D tissue culture. Here, we demonstrate the use of molecular parameters (HA M_w and degree of BZA functionalization) to control the viscoelasticity of DCC hydrogels while still allowing for week-long culture experiments.

Specifically, by varying only the HA M_w in our HELP system, we investigated the effects of mismatched polymer sizes (HA vs. ELP) on gel stress relaxation and stiffness behavior. As expected, higher molecular weight typically led to higher gel stiffness (G'). Longer polymers have a greater number of potential crosslinking sites per chain, and hence a larger number of possible percolating paths through the network [48]. Interestingly, we observed that the mismatched polymer sizes strongly influence the network stress-relaxation rates. Varying HA M_w had a parabolic effect on the relaxation rate of the gels: formulations with high HA M_w (500 kDa) relaxed as fast as low HA M_W (20 kDa). To understand this, we developed and validated an empirically-based modified Maxwell Model of gel viscoelasticity, in which we include the ratio of polymer molecular weight, $q = M_{wHA}/M_{wELP}$, as a normalizing parameter. This model fits the behavior of all formulations with low and intermediate HA M_w, where their relaxation behavior collapses into a single trendline when normalized by q. However, this empirical model fails to replicate the behavior of the high HA

M_w formulation (500 kDa), suggesting additional mechanisms of relaxation are in place when the polymers are highly mismatched in size, likely driven by entanglement movement. The increased presence of entanglements was validated through the strain overshoot behavior seen in LAOS in highly mismatched formulations; however, future studies to acquire structural information through analysis such as SAXS would be beneficial in further understanding this phenomenon. In addition, the presence of this secondary relaxation mode is supported by the analysis of the relative sizes of the polymers in solution, as the difference in size scales exponentially with the mismatch parameter q. Thus, long polymers lead to different semi-dilute regimes, allowing more crowded, entangled solutions and additional relaxation mechanisms. The relaxation of HELP gels is further tunable through the degree of functionalization of BZA on our HA chain, with increasing functionalization leading to slower-relaxing hydrogels due to the increase in crosslinking density. While our modified Maxwell model captures this increase in elasticity in low and intermediate HA M_w, it again fails to explain the behavior at very high HA M_w ($\geq$ 500 kDa). To address this, we introduced the Two-Polymer DCC Network model, where, in addition to the q parameter, we added a second spring-dashpot to represent a secondary mode of relaxation. This phenomenological framework was able to describe the viscoelastic behavior of all characterized HELP gel formulations across the full ranges of HA M_w and degree of functionalization that were tested. Thus, this phenomenological model provides a helpful conceptual understanding in which to predict the viscoelastic behavior of HELP gels. As DCC gels can be designed using a variety of different polymer backbones and crosslink chemistries, an exciting area for future study is to explore if the Two-Polymer DCC Network model developed here can also describe the viscoelastic behavior of other DCC gels. For example, DCC hydrogels with alternative kinetics, such as oxime and imine bonds, as well as alternative polymer backbones, such as alginate or polyethylene glycol, can be studied to explore the applicability of the theoretical framework described here.

Given the importance of gels as 3D in vitro tissue culture systems, we then demonstrated the applicability of these formulations to culture hiPSC-NPC for one week. As a key advantage, we were able to keep the crosslinking chemistry (and hence crosslinking reaction kinetics) constant across all formulations, resulting in gels that were sufficiently stable for multi-day culture. By separately modulating the stiffness and relaxation rate, we observed that softer gels (G' ≈200 Pa) with intermediate to fast stress-relaxation rates lead to higher expression of a stemness marker and increased neurite outgrowth. Interestingly, we also observed that gels formulated with high HA M_w (500 kDa) correlated with increased formation of cell clusters (i.e., neurospheres), suggesting that secondary relaxation modes may also influence cell phenotype. Cells can "sense" the viscoelastic properties of their surrounding matrix through several different mechanisms; thus, this family of modular gels is well suited for future studies of the mechanisms of cellular mechanosignaling [24, 30, 31].

In summary, this work expands the molecular design space of DCC hydrogels to achieve tunable viscoelasticity for 3D in vitro models, decreasing our reliance on bond kinetics and improving our conceptual understanding of relaxation modes. Given the large design space of DCC hydrogels and their ability to support long-term culture of human cells, these materials are well suited to replace and complement animal studies of disease progression and drug discovery in the future.

4 | Experimental

4.1 | Materials

All reagents were purchased from Sigma–Aldrich and used without further purification, unless otherwise noticed.

4.1.1 | Synthesis of Elastin-Like Protein

The ELP was synthesized through recombinant protein expression as previously described [28]. Briefly, ELP encoding plasmids were transformed into BL21(DE3) pLysS *Escherichia coli* (Life Technologies). The bacteria were grown in Terrific Broth at 37 °C. When the OD600 reached a value of 0.8, the ELP expression was induced with an 1 mM of isopropyl β-d-1-thiogalactopyranoside (Fisher) and the expressed proceeded for 7 h. Subsequently, the bacteria were pelleted and resuspended in TEN Buffer (10 mM Tris (Fisher), 1 mM ethylenediamine tetraacetic acid disodium salt dihydrate (EDTA, Fisher), and 100 mM NaCl (Fisher), pH 8.0) [28]. Alternating freeze and thaw cycles were used to lyse the cell pellet. Deoxyribonuclease and phenylmethylsulphonyl fluoride were added to the cell lysate at 1 mM [28]. ELP was purified through thermocycling followed by dialysis in deionized water (DI) with 6 water changes, having a minimum residence time of 6 h in-between changes, at 4°C. The purified protein was lyophilized and stored at −20°C [28].

4.1.2 | Functionalization and Characterization of ELP-HYD

The ELP was modified following previously published protocols [32, 34]. In short, a hexafluorophosphate azabenzotriazole tetramethyl uronium (HATU) enabled amidation reaction was used to modify the amine on he lysine amino acid of the ELP. The lyophilized ELP was dissolved in a solution of equal volumes (3% (w/v)) of anhydrous dimethyl sulfoxide (DMSO) and *N*,*N*-dimethylformamide (DMF) [28]. In a separate vessel, tri-boc hydrazinoacetic acid was dissolved at 2.1% (w/v) in anhydrous DMF, at room temperature. The dissolved tri-boc was activated with HATU (2.0 equivalence per ELP amine; Sigma, 445460) and 4-methylmorpholine (NMM, 5 equivalence per ELP amine) for 10 min [28]. The activated tri-boc molecule was added to the ELP solution dropwise under continuous stirring, and the reaction was left to proceed overnight [28]. The tri-boc modified protein was precipitated in ice-cold diethyl ether in a 1:4 volume ratio of reaction solution to ether [28]. The product was pelleted and dried under nitrogen for 3 days [28]. In order to deprotect the hydrazine group, the pellet was resuspended in a solution of equal volumes of dichloromethane (DCM) and trifluoroacetic acid supplemented with 5% (v/v) tri-isopropylsilane (Sigma, 233781). After 4 h the deprotected ELP-HYD was precipitated in ether, dried under nitrogen for 3 days, and resuspended in DI water at 4 °C [28]. The protein was dialyzed against DI water with 6 water changes, having a minimum residence time of 6 hours in-between changes at 4 °C. The resulting solution was sterile

filtered (0.22 μm) in a biosafety cabinet, lyophilized, and stored at −20 °C.

4.1.3 | Functionalization and Characterization of Hyaluronic Acid with Benzaldehyde (HA-BZA) or Aldehyde (HA-ALD)

HA of different MW were purchased from Lifecore: HA20K-1, HA40K-1, HA60K-1, HA100K-1, HA500K-1, HA1M-1 (viscosity-averaged MW of each HA as reported by Lifecore is listed in Figure S9). To evaluate the PDI and confirm the measurements provided by Lifecore, we previously reported gel permeation chromatography on these reagents (Figure S9). Depending on the measurement method, due to the polydispersity of these samples, the viscosity-averaged, weight-averaged, and number-averaged molecular weights will all be slightly different. HA was functionalized following previously published protocols [28]. First, HA of different molecular weights (LifeCore, HA20K-1, HA40K-1, HA60K-1, HA100K-1, HA500K-1, HA1M-1) was modified with an alkyne group through an EDC/NHS reaction at different equivalences depending upon the desired final BZA or ALD functionalization (1 eq. for 6% and 12% functionalization, 3 eq. for 20% functionalization) [28]. The reaction proceeded at room temperature overnight. The final mixture was dialyzed against DI water with 6 water changes, having a minimum residence time of 6 hours in-between changes. After dialysis, the mixture was filtered through a 0.22 μm filter and subsequently lyophilized.

To achieve HA-BZA or HA-ALD, a copper-catalized azide-alkyne cycloaddition, also known as a copper-click reaction was performed on the HA–alkyne. Briefly, the HA-alkyne solid was dissolved in isotonic 10× PBS (10× iPBS) (81 mM sodium phosphate dibasic, 19 mm sodium phosphate monobasic, 60 mM sodium chloride in Milli-Q water; pH adjusted to 7.4; 0.22 μm filtered) supplemented with β-cyclodextrin at a 1 mg mL^{-1} [28]. Stock solutions of 2.4 mm copper sulfate (Copper sulfate, 5-hydrate – JT Baker 1841-01) and 45.2 mm sodium ascorbate were prepared [28]. All solutions were degassed for 30 min under nitrogen flow. Finally, azido-BZA or azido-ALD (Santa Cruz Biotechnology) was dissolved in extra dry DMSO (Acros Organics 61097-1000) depending on the targeted BZA or ALD functionalization: 1 eq. with respect to the corresponding HA–alkyne for 6% functionalization, and 2 eq. for 12% and 20% functionalization [28]. The reagents were added to the solution as previously described, and the reaction proceeded for 24 h at room temperature [28]. Then, the reaction stopped by chelating the copper with 50 mM EDTA (Fisher O2793-500) [28]. Last, the mixture was dialyzed, filtered, and lyophilized as previously described. The degree of functionalization of HA-BZA was evaluated through ^{1}H NMR [20, 77], and the different degrees of functionalization were quantified, resulting in 6% ± 3%, 12% ± 3%, and 20% ± 3% (Figure S1).

4.1.4 | Functionalization Hyaluronic Acid with Hydrazine (HA-HYD)

First a N-(3-azidopropyl)-2-hydrazineylacetamide was synthesized as previously published [78]. Briefly, a dimethylaminopyridine (0.2 eq.) catalyzed EDC (1.3 eq.) reaction was performed in DCM by combining tri-Boc hydrazinoacetic acid (1 eq.) with azidopropyl amine (1.3 eq). The reaction proceeded overnight under continuous stirring. Following the reaction, the solvent was removed through a rotary evaporator, and the molecule was purified through silica gel chromatography. The protecting Boc groups were then removed by solubilizing the material in 1:1 DCM/TFA mixture for 4 h, and the final N-(3-azidopropyl)-2-hydrazineylacetamide (azido-HYD) was precipitated into ether [78]. Following this synthesis, HA-60kDa was functionalized with hydrazine group following the same protocol used to achieve HA-BZA, except the azido-BZA was substituted with azido-HYD as the functionalizing motif. All equivalences were the same ones applied to achieve 12% HA functionalization.

4.1.5 | Hydrogel Formation

All HELP hydrogels have a final composition of 1 wt.% ELP-HYD and 1 wt% HA-BZA or HA-ALD in 10× iPBS, regardless of the HA molecular weight or degree of functionalization. The components, HA-BZA or HA-ALD and ELP-HYD, were dissolved at a stock concentration of 2 wt.% in 10× iPBS overnight at 4 °C under continuous rotation. Equal volumes of 2 wt.% HA-BZA or HA-ALD and 2 wt.% ELP-HYD were mixed on ice, to prevent ELP aggregation. This procedure allowed for the hydrazone crosslinks to spontaneously form, creating gels with final concentration of 1 wt.% HA and 1 wt.% ELP.

4.2 | Rheometry

Rheological characterization was performed on an ARG2 rheometer (TA Instruments) equipped with a Peltier plate using a 20-mm cone-plate geometry with an angle of 1 °. All rheology was performed on gels crosslinked directly on the rheometer stage, as this yields the most consistent and high-quality data. It is important to highlight that different solvents (e.g. water, phosphate-buffered saline, specific different cell culture media, in vivo interstitial fluid, etc.) will each impact hydrogel swelling behavior differently, which can directly impact entanglements and accessibility of crosslinking groups. As a consequence, we used an on-stage crosslinking protocol to yield reliable data that can be compared across different research groups and across different formulations, regardless of intended downstream application.

The two components of the HELP hydrogels (ELP-HYD and HA-BZA or HA-ALD) were pre-mixed in an 0.6 mL Eppendorf tube and loaded onto the rheometer with the measurement starting 10 s after mixing. The gelation was monitored through a time-oscillation measurement at an angular frequency (ω) of 1 rad s^{1-} and a shear strain amplitude (γ) of 1 %. The gel is loaded on the rheometer and kept at 4 °C for 5 min. Subsequently the temperature is ramped to 23 °C at a heating rate of 3 °C min^{-1} and the measurement continues isothermal for 15 min. The temperature was then ramped to 37 °C at a heating rate of 3 °C min^{-1} and the measurement continues isothermal for 15 min. Finally, frequency-sweep, from 0.01 to 250 rad/s, was performed at a shear strain amplitude of 1 % at 37 °C. The sample then remained at 37 °C at a 1.0 % strain for 5 min. A step stress relaxation at a constant shear strain amplitude of 10 % was

performed, and relaxation was followed for at least 12 h. Each experimental condition was measured in at least triplicates, $n \geq 3$. In relaxation profile plots, the normalized data is presented as the average and shaded area represents the standard deviation. To test for potential interactions between unmodified ELP and HA, we performed rheology on a mixture of HA and ELP (both at 1 wt.%, similar to our hydrogel formulations), and no gelation was observed (Figure S10).

4.3 | Modeling

All modeling was performed through Matlab R2025a. First, all exported files were separated into each of the rheometry steps, and the stress relaxation step was isolated. Each stress relaxation experiment was normalized with respect to initial stress and smoothed through a standard moving average algorithm. Once normalized, the average stress relaxation profile was calculated for each experimental condition for the first 12 h of relaxation. To assess the characteristic relaxation time (τ_0) at $q = 1$ (40 kDa-HA), the normalized averaged relaxation data of this condition was fitted to the Modified Maxwell Model, $[k_e + k_1 exp(-\frac{t}{\tau_0})]$, where k_e, k_1, and τ_0 were optimized fitting parameters, finding the $\tau_0 \approx 28661$. Then, all conditions were fitted to the Modified Maxwell Model with a their respective set $\tau_\epsilon = q \cdot \tau_0$, and k_e, k_1 were the optimized fitting parameters. When fitting the Two-Component DCC Network model, $[k_e + k_1 exp(-\frac{t}{q \cdot \tau_0}) + k_2 exp(-\frac{t}{\tau_{\epsilon 2}})]$, the same set τ_ϵ was maintained, and k_e, k_1, k_2, and $\tau_{\epsilon 2}$ were the optimized fitting parameters. All averaged empirical data was fitted to the corresponding models through a non-linear least-squares local solver, *'lsqcurvefit'*, which was run 500 times, through a GlobalOptimSolution combined with a MultiStart, to ensure the optimal solution despite potential multiple local minima. As the fitted parameters are representative of physical properties, all fitting parameters (k_e, k_1, k_2, and $\tau_{\epsilon 2}$) were constrained to be ≥ 0.

4.4 | iPSC-hNPC Differentiation and Encapsulation

We differentiated human induced pluripotent stem cells (hiPSCs) into neural progenitor cells through a dual SMAD inhibition kit (Stem Cell Technologies) [30]. After 13 days of differentiation, we dissociated all cells with Accutase (Sigma-Aldrich), and passaged onto plates coated with poly-d-lysine (50 μg/mL; Sigma-Aldrich) and laminin (10 μg/mL; Roche) [30]. From day 13 onward, the differentiated NPCs were maintained in N3 culture medium, which is composed of 1:1 DMEM/F12 (Thermo Fisher):Neurobasal (Thermo Fisher), N2 supplement (1%, Thermo Fisher), B27 supplement (2%, Thermo Fisher), GlutaMAX (1%, Thermo Fisher), MEM non-essential amino acids (1%, Thermo Fisher), and Penicillin–Streptomycin (1%, Thermo Fisher) [30].

All NPCs were encapsulated on days 18–22 of differentiation. Before encapsulation, the cells were dissociated with Accutase, pelleted by centrifugation, and counted. The NPC pellets were resuspended in 2 wt.% ELP-HYD solution at two times the selected final cell density within the gel (i.e., 60,000 cells/μL for a final cell density of 30,000 cells/μL). The cell suspensions were thoroughly mixed with the selected 2 wt.% HA-BZA solution, and 10 μL gels were cast in 4 mm diameter, 0.8 mm height silicone molds. The molds were placed into 24-well plates [30]. The gels crosslinked for 5 min on ice, 15 minutes at room temperature (RT), and 10 min at 37 °C. Then, we added the N3 media supplemented with 10 μM Y27632 (Tocris Biosciences) [30]. Fresh media without Y276332 was replenished the next day. Media changes were performed daily for 7 days.

4.5 | Cell Viability

At day 7 (end-point), Live/Dead kit (Invitrogen) was used to assess cell viability at 37 °C. Encapsulated gels were washed in phosphate buffered saline (PBS, Invitrogen) for 5 min per wash for three washes total, and incubated with 4.0 μM calcein-AM and 4.0 μM ethidium homodimer-1 in PBS for 30 min [21]. All samples were rinsed in PBS, and imaged on a confocal microscope (Leica STELLARIS 5) at 10x and 20x magnification. Z-stacks of 100 – 150 μm height were taken with 10-μm z-steps at three different locations in each hydrogel, Figure S11 [21].

4.6 | Immunocytochemistry

At the end-point, the gel-encapsulated cells were fixed in 4% paraformaldehyde in PBS for 20 min at RT. The samples were then washed three times with PBS and stored at 4 °C until use. The fixed samples were permeabilized with 0.25% (v/v) Triton X-100 in PBS (PBS-T) for 1 hour at RT and then blocked with 5% (w/v) bovine serum albumin (BSA; Roche), 5% (v/v) goat serum (Gibco), and 0.5% Triton X-100 in PBS for 3 h at RT [30]. An antibody solution was prepared in PBS with 2.5% (w/v) BSA, 2.5% (v/v) goat serum, and 0.5% (v/v) Triton X-100. The following primary antibodies were used accross all conditions: mouse anti-β3-tubulin (1:400, Cell Signaling, mAb 4466) and rabbit anti-Sox2 (1:400, Cell Signaling, mAb 23064). Primary antibody incubation was performed for 48 h at 4 °C. After two nights, all samples were washed three times with PBS-T for 30 min each, and then secondary antibodies were diluted in antibody dilution solution as follows: goat anti-rabbit Alexa Fluor 488 (1:500, Invitrogen, A-11008), goat anti-mouse Alexa Fluor 555 (1:500, Invitrogen, A-21422). 4',6-diamidino-2-phenylindole (DAPI; 1 μg/mL, Cell Signaling, 4083s) was included to stain for nuclei [30]. Secondary antibodies were incubated overnight at 4 °C. The following day, samples were washed three times with PBS-T for 20 min each and then mounted onto #1 coverslips with ProLong Gold AntiFade Mountant (Thermo Fisher) [30]. After curing for 24 h, stained hydrogels were imaged with a confocal microscope (Leica STELLARIS 5, Las-X software). All images were taken at a z-depth of at least 50 μm from the coverslips to avoid possible confounds imparted by the mechanical properties of the glass. Z- stacks of 250 μm height were taken with 10-μm z-steps at five different locations in each hydrogel [30].

4.7 | Image Analysis

All in vitro experiments were performed in 3 independent gel/cell experimental replicates, out of which N = 10 randomly selected

fields-of-view from 2 gels were quantified. The length of individual neurites was characterized by manually tracing TUBB3-expressing projections, and quantified with the SNT toolbox, where each cell represents one data point (n), Table S17 [23, 29, 79–81]. Cluster size was quantified using CellProfiler based on DAPI staining, identifying objects > 40 pixel units in diameter using no method to distinguish between clumped objects. CellProfiler was also used to quantified the number of Sox2+ cells and area occupied by TUBB3+ neurites [30]. Briefly, nuclei and cells were immunolabeled with the relevant markers or antibodies and identified using"IdentifyPrimaryObjects" with the"Minimum Cross-Entropy" thresholding method. TUBB3-labeled neurites were identified by passing the TUBB3 images through "EnhanceOrSuppressFeatures", "IdentifyPrimaryObjects", and "MeasureImageAreaOccupied" [30]. All quantification on a per cell basis was done by normalizing either the Sox2 count or the area of TUBB3 expression by nuclei count.

4.8 | Hydrogel Erosion

Each biological environment possesses different ionic strengths, amounts of proteins and polysaccharides, and levels of proteases, all of which will impact erosion and potential enzymatic degradation [78, 82, 83]. To assess solely the passive erosion caused by crosslink exchange and polymer chain diffusion into the supernatant, rather than enzymatic degradation, this study was performed with PBS, a common reagent in cell culture laboratories, as a standardized manner to assess erosion. For the erosion study, gels with a volume of 40 μL were cast in the bottom of 0.5 mL Eppendorf tubes following the protocol described above. After gelation, 200 μL of PBS was added on top of the gels and the Eppendorfs were closed, and incubated at 37 °C. The entire volume of supernatant was removed and replaced at each experimental timepoint, and the supernatant stored at −80 °C prior to analysis. A uronic assay was used to quantify the amount of HA released into the supernatant, as described earlier [84]. Unmodified HA samples of the same M_w were used as standards and PBS-filled wells used to blank the readings.

4.9 | Hydrogel Swelling

As hydrogel swelling can impact rheological properties, we performed a swelling test on our HELP formulation in comparison with HA-only formulation using a 60-kDa HA-BZA with 12% functionalization, combined with either an ELP-HYD or an 60-kDa HA-HYD. We weighted empty 4-mm silicone molds before casting any gel. All gels were casted at a total volume of 10 µL, and dried overnight under vacuum. The mass of each dried sample was measured, and the sample was incubated in 1 mL of PBS for 3 h at room temperature. After incubation, the mass of the swollen sample was measured. Overall, the HELP formulations displayed a significantly lower increase in normalized swelling ratio post-incubation, Figure S12. This suggests HELP formulations have relatively low swelling when compared to other common polymeric formulations, presumably due to ELP aggregation. Further, it supports that prior to optimization for a specific, intended biomedical use, swelling studies and rheological measurements should be performed on gels swollen with the relevant, appropriate biological solution.

4.10 | Statistical Analysis

For all figures, except Figure 6E,F, data are presented as the mean and standard deviation. Individual replicates are represented as symbols points, where appropriate. Prior to significance testing, normality and equality of variance were tested with Shapiro–Wilks, Normal QQ plots, and Brown–Forsythe at significance level 0.05, respectively. All data were analyzed through an one-way ANOVA, and Tukey's post hoc means comparison at significance level 0.05. Data on Figure 6E-F are not normally distributted. Thus, it was analyzed by a Kruskal–Wallis with Dunn's post hoc means comparison at significance level 0.05. All significance is denoted as $^*p < 0.05$, $^{**}p < 0.01$, $^{***}p < 0.001$, $^{****}p < 0.0001$, and ns as not significant. All analysis was performed with GraphPad Prism10.

Acknowledgments

The authors thank Pedro Pinheiro for assistance with the code implementation, Prof. Gerald G. Fuller for helpful discussion, Dr. Patrik K. Johansson for assistance with image aquisition and Centaine S. Joseph for assistance with swelling test. This work was supported by the National Science Foundation (NSF) grants DGE-1656518 (N.J.B. and M.S.H.) and DMR-2427971 (S.C.H.); the National Institutes of Health (NIH) grants F31-HL175888 (N.J.B.), F31-NS132505 (M.S.H.), and R01-EY035697, R01-HL173056, R01-MH137333 (S.C.H.); Stanford Cardiovascular Institute seed grant (S.C.H.); the ARCS Foundation Scholarship (N.J.B.); the PhRMA Foundation Predoctoral Fellowship in Drug Delivery (N.J.B.); the American Heart Association (AHA) Predoctoral Fellowship (24PRE1191604) (N.d.P.N.); the Gerald J. Lieberman Fellowship (N.d.P.N, and M.S.H.); the Swiss National Science Foundation Postdoc Mobility Fellowship (PN210723) (F.C.); the Sarafan ChEM-H Chemistry-Biology Interface Program (M.S.H.); and Fundación Alfonso Martin Escudero Fellowship (C.H.L.).

Conflicts of Interest

The authors declare no conflicts of interest.

Data Availability Statement

The data that support the findings of this study are openly available in Stanford Digital Repository at https://doi.org/10.25740/hg746sr4717. All MATLAB code can be found at https://github.com/narellinpn/Tuning-Viscoelasticity-of-Dynamic-Covalent-Hydrogels---AFM.git

References

1. M. W. Tibbitt and K. S. Anseth, "Hydrogels as Extracellular Matrix mimics for 3D Cell Culture," *Biotechnology and Bioengineering* 103 (2009): 655–663, https://doi.org/10.1002/bit.22361.

2. F. Xu, C. Dawson, M. Lamb et al., "Hydrogels for Tissue Engineering: Addressing Key Design Needs Toward Clinical Translation," *Frontiers in Bioengineering and Biotechnology* 10 (2022): 849831, https://doi.org/10.3389/fbioe.2022.849831.

3. Z. Terzopoulou, A. Zamboulis, I. Koumentakou, G. Michailidou, M. J. Noordam, and D. N. Bikiaris, "Biocompatible Synthetic Polymers for Tissue Engineering Purposes," *Biomacromolecules* 23 (2022): 1841–1863, https://doi.org/10.1021/acs.biomac.2c00047.

4. C. M. Leung, P. de Haan, K. Ronaldson-Bouchard et al., "A Guide to the Organ-on-a-Chip," *Nature Reviews Methods Primers* 2 (2022): 33.

5. Y. Huang, T. Liu, Q. Huang, and Y. Wang, "From Organ-on-a-Chip to Human-on-a-Chip: A Review of Research Progress and Latest Applications," *ACS sensors* 9 (2024): 3466–3488.

6. D. E. Ingber, "Human Organs-on-Chips for Disease Modelling, Drug Development and Personalized Medicine," *Nature Reviews Genetics* 23, no. 8 (2022): 467–491.

7. M. S. Huang, F. Christakopoulos, J. G. Roth, and S. C. Heilshorn, "Organoid Bioprinting: From Cells to Functional Tissues," *Nature Reviews Bioengineering* 3 (2025): 126–142, https://doi.org/10.1038/s44222-024-00268-0.

8. J. Kim, B. K. Koo, and J. A. Knoblich, "Human Organoids: Model Systems for Human Biology and Medicine," *Nature Reviews Molecular Cell Biology* 21, no. 10 (2020): 571–584.

9. X. Y. Tang, S. Wu, D. Wang et al., "Human Organoids in Basic Research and Clinical Applications," *Signal Transduction and Targeted Therapy* 7, no. 12 (2022): 168.

10. X. Liu, Z. Zhou, Y. Zhang, H. Zhong, X. Cai, and R. Guan, "Recent Progress on the Organoids: Techniques, Advantages, and Applications," *Biomedicine & Pharmacotherapy* 185 (2025): 117942.

11. W. H. Abuwatfa, W. G. Pitt, and G. A. Husseini, "Scaffold-Based 3D Cell Culture Models in Cancer Research," *Journal of Biomedical Science* 31 (2024): 7.

12. A. Elosegui-Artola, A. Gupta, A. J. Najibi et al., "Matrix Viscoelasticity Controls Spatiotemporal Tissue Organization," *Nature Materials* 22 (2023): 117–127, https://doi.org/10.1038/s41563-022-01400-4.

13. O. Chaudhuri, L. Gu, M. Darnell et al., "Substrate Stress Relaxation Regulates Cell Spreading," *Nature Communications* 6 (2015): 6365, https://doi.org/10.1038/ncomms7365.

14. O. Courbot and A. Elosegui-Artola, "The Role of Extracellular Matrix Viscoelasticity in Development and Disease," *npj Biological Physics and Mechanics* 2 (2025): 10, https://doi.org/10.1038/s44341-025-00014-6.

15. D. Huang, Y. Huang, Y. Xiao et al., "Viscoelasticity in Natural Tissues and Engineered Scaffolds for Tissue Reconstruction," *Acta biomaterialia* 97 (2019): 74–92.

16. X. Dai, D. Wu, K. Xu, P. Ming, S. Cao, and L. Yu, "Viscoelastic Mechanics: From Pathology and Cell Fate to Tissue Regeneration Biomaterial Development," *ACS Applied Materials & Interfaces* 17 (2025): 8751–8770.

17. N. Cheng, Y. Zhang, Y. Wu et al., "Hydrogel Platform Capable of Molecularly Resolved Pulling on Cells for Mechanotransduction," *Materials Today Bio* 17 (2022): 100476, https://doi.org/10.1016/j.mtbio.2022.100476.

18. E. Hachet, H. Van Den Berghe, E. Bayma, M. R. Block, and R. Auzely-Velty, "Design of Biomimetic Cell-Interactive Substrates Using Hyaluronic Acid Hydrogels with Tunable Mechanical Properties," *Biomacromolecules* 13, no. 6 (2012): 1818–1827, https://doi.org/10.1021/bm300324m.

19. D. R. Hunt, K. C. Klett, S. Mascharak et al., "Engineered Matrices Enable the Culture of Human Patient-Derived Intestinal Organoids," *Advanced Science* 8, no. 10 (2021): 2004705, https://doi.org/10.1002/advs.202004705.

20. B. L. LeSavage, D. Zhang, C. Huerta-López et al., "Engineered Matrices Reveal Stiffness-Mediated Chemoresistance in Patient-Derived Pancreatic Cancer Organoids," *Nature Materials* 23, no. 8 (2024): 1138–1149, https://doi.org/10.1038/s41563-024-01908-x.

21. R. S. Navarro, M. S. Huang, J. G. Roth et al., "Tuning Polymer Hydrophilicity to Regulate Gel Mechanics and Encapsulated Cell Morphology," *Advanced Healthcare Materials* 11, no. 13 (2022): e2200011, https://doi.org/10.1002/adhm.202200011.

22. M. Darnell, S. Young, L. Gu et al., "Substrate Stress-Relaxation Regulates Scaffold Remodeling and Bone Formation In Vivo," *Advanced Healthcare Materials* 6 (Jan 2017), https://doi.org/10.1002/adhm.201601185.

23. O. Chaudhuri, L. Gu, D. Klumpers et al., "Hydrogels with Tunable Stress Relaxation Regulate Stem Cell Fate and Activity," *Nature Materials* 15 (March 2016): 326–334, https://doi.org/10.1038/nmat4489.

24. O. Chaudhuri, J. Cooper-White, P. A. Janmey, D. J. Mooney, and V. B. Shenoy, "Effects of Extracellular Matrix Viscoelasticity on Cellular Behaviour," *Nature* 584 (2020): 535–546.

25. Y. Liu, A. E. Gilchrist, P. K. Johansson et al., "Engineered Hydrogels for Organoid Models of Human Nonalcoholic Fatty Liver Disease," *Advanced Science* 12 (2025): e17332, https://doi.org/10.1002/ADVS.202417332.

26. S. M. Hull, J. Lou, C. D. Lindsay et al., "3D Bioprinting of Dynamic Hydrogel Bioinks Enabled by Small Molecule Modulators," *Science Advances* 9, no. 13 (2023): eade7880, https://doi.org/10.1126/sciadv.ade7880.

27. A. N. Borelli, M. W. Young, B. E. Kirkpatrick et al., "Stress Relaxation and Composition of Hydrazone-Crosslinked Hybrid Biopolymer-Synthetic Hydrogels Determine Spreading and Secretory Properties of MSCs," *Advanced Healthcare Materials* 11, no. 14 (2022): 2200393, https://doi.org/10.1002/adhm.202200393.

28. N. de Paiva Narciso, R. S. Navarro, A. E. Gilchrist, M. L. Trigo, G. A. Rodriguez, and S. C. Heilshorn, "Design Parameters for Injectable Biopolymeric Hydrogels with Dynamic Covalent Chemistry Crosslinks," *Advanced Healthcare Materials* 12 (2023): 2301265, https://doi.org/10.1002/adhm.202301265.

29. J. G. Roth, M. S. Huang, R. S. Navarro, J. T. Akram, B. L. Lesavage, and S. C. Heilshorn, "Tunable Hydrogel Viscoelasticity Modulates Human Neural Maturation," *Science Advances* 9, no. 42 (2023): eadh8313, https://doi.org/10.1126/sciadv.adh8313.

30. M. S. Huang, B. L. LeSavage, S. Ghorbani et al., "Viscoelastic N-Cadherin-Like Interactions Maintain Neural Progenitor Cell Stemness within 3D Matrices," *Nature Communications* 16 (2025): 5213, https://doi.org/10.1038/s41467-025-60540-8.

31. R. A. Suhar, M. S. Huang, R. S. Navarro, G. A. Rodriguez, and S. C. Heilshorn, "A Library of Elastin-Like Proteins with Tunable Matrix Ligands for In Vitro 3D Neural Cell Culture," *Biomacromolecules* 24 (2023): 5926–5939, https://doi.org/10.1021/acs.biomac.3c00941.

32. M. E. Hefferon, M. S. Huang, Y. Liu et al., "Cell Microencapsulation Within Engineered Hyaluronan Elastin-Like Protein (HELP) Hydrogels," *Current Protocols* 3 (2023): e917, https://doi.org/10.1002/cpz1.917.

33. H. Wang, A. Paul, D. Nguyen, A. Enejder, and S. C. Heilshorn, "Tunable Control of Hydrogel Microstructure by Kinetic Competition between Self-Assembly and Crosslinking of Elastin-like Proteins," *ACS Applied Materials Interfaces* 10, no. 26 (2018): 21808–21815, https://doi.org/10.1021/acsami.8b02461.

34. B. L. LeSavage, N. A. Suhar, C. M. Madl, and S. C. Heilshorn, "Production of Elastin-like Protein Hydrogels for Encapsulation and Immunostaining of Cells in 3D," *Journal of Visualized Experiments*, no. 135 (2018): 57739, https://doi.org/10.3791/57739.

35. X. Xu, A. K. Jha, D. A. Harrington, M. C. Farach-Carson, and X. Jia, "Hyaluronic Acid-Based Hydrogels: from a Natural Polysaccharide to Complex Networks," *Soft Matter* 8, no. 12 (2012): 3280–3294, https://doi.org/10.1039/C2SM06463D.

36. C. M. Madl and S. C. Heilshorn, "Bioorthogonal Strategies for Engineering Extracellular Matrices," *Advanced Functional Materials* 28, no. 11 (2018), https://doi.org/10.1002/adfm.201706046.

37. V. Zhang, J. V. Accardo, I. Kevlishvili et al., "Tailoring Dynamic Hydrogels by Controlling Associative Exchange Rates," *Chem* 9 (Aug 2023): 2298–2317, https://doi.org/10.1016/j.chempr.2023.05.018.

38. S. Hafeez, H. W. Ooi, F. L. C. Morgan et al., "Viscoelastic Oxidized Alginates with Reversible Imine Type Crosslinks: Self-Healing, Injectable, and Bioprintable Hydrogels," *Gels* 4, no. 4 (2018), https://doi.org/10.3390/gels4040085.

39. Y. Han, Y. Cao, and H. Lei, "Dynamic Covalent Hydrogels: Strong yet Dynamic," *Gels* 8, no. 9 (2022), https://doi.org/10.3390/gels8090577.

40. K. S. Anseth and H. A. Klok, "Click Chemistry in Biomaterials, Nanomedicine, and Drug Delivery," *Biomacromolecules* 17, no. 1 (2016): 1–3, https://doi.org/10.1021/acs.biomac.5b01660.

41. V. G. Muir and J. A. Burdick, "Chemically Modified Biopolymers for the Formation of Biomedical Hydrogels," *Chemical Review* 121, no. 18 (2021): 10908–10949, https://doi.org/10.1021/acs.chemrev.0c00923.

42. Y. Liu, A. E. Gilchrist, and S. C. Heilshorn, "Engineered Protein Hydrogels as Biomimetic Cellular Scaffolds," *Advanced Materials* 36, no. 45 (2024): 2407794, https://doi.org/10.1002/adma.202407794.

43. J. Stiles and T. L. Jernigan, "The Basics of Brain Development," *Neuropsychology Review* 20 (2010): 327–348.

44. D. D. Liu, J. Q. He, R. Sinha et al., "Purification and Characterization of Human Neural Stem and Progenitor Cells," *Cell* 186 (March 2023): 1179–1194, e15, https://doi.org/10.1016/j.cell.2023.02.017.

45. D. D. McKinnon, D. W. Domaille, J. N. Cha, and K. S. Anseth, "Bio-Physically Defined and Cytocompatible Covalently Adaptable Networks as Viscoelastic 3D Cell Culture Systems," *Advance Materials* 26, no. 6 (2014): 865–872, https://doi.org/10.1002/adma.201303680.

46. Y.-H. Lin, J. Lou, Y. Xia, and O. Chaudhuri, "Cross-Linker Architectures Impact Viscoelasticity in Dynamic Covalent Hydrogels," *Advanced Healthcare Materials* 13, no. 30 (2024): 2402059, https://doi.org/10.1002/adhm.202402059.

47. M. W. Jaeschke, A. N. Borelli, N. P. Skillin, T. J. White, and K. S. Anseth, "Engineering a Hydrazone and Triazole Crosslinked Hydrogel for Extrusion-Based Printing and Cell Delivery," *Advanced Healthcare Materials* 13, no. 20 (2024): 2400062, https://doi.org/10.1002/adhm.202400062.

48. P. C. Cai, B. Su, L. Zou, M. J. Webber, S. C. Heilshorn, and A. J. Spakowitz, "Rheological Characterization and Theoretical Modeling Establish Molecular Design Rules for Tailored Dynamically Associating Polymers," *ACS Central Science* 8 (2022): 1318–1327, https://doi.org/10.1021/acscentsci.2c00432.

49. J. K. Jackson, M. E. de Rosa, and H. H. Winter, "Molecular Weight Dependence of Relaxation Time Spectra for the Entanglement and Flow Behavior of Monodisperse Linear Flexible Polymers," *MacroMolecules* 27, no. 9 (1994): 2426–2431, https://doi.org/10.1021/ma00087a010.

50. M. E. D. Rosa and H. H. Winter, "The effect of entanglements on the rheological behavior of polybutadiene critical gels," *Rheologica Acta* 33 (1994): 220–237, https://doi.org/10.1007/BF00437307.

51. C. Oelschlaeger, M. Cota Pinto Coelho, and N. Willenbacher, "Chain Flexibility and Dynamics of Polysaccharide Hyaluronan in Entangled Solutions: A High Frequency Rheology and Diffusing Wave Spectroscopy Study," *Biomacromolecules* 14, no. 10 (2013): 3689–3696, https://doi.org/10.1021/bm4010436.

52. P. G. de Gennes, "Reptation of a Polymer Chain in the Presence of Fixed Obstacles," *The Journal of Chemical Physics* 55, no. 2 (Aug 1971): 572–579, https://doi.org/10.1063/1.1675789.

53. P. C. Cai, B. A. Krajina, and A. J. Spakowitz, "Brachiation of a Polymer Chain in the Presence of a Dynamic Network," *Physical Review E* 102, no. 2-1 (2020): 020501, https://doi.org/10.1103/PhysRevE.102.020501.

54. O. Chaudhuri, "Viscoelastic Hydrogels for 3D Cell Culture," *Biomaterials Science* 5, no. 8 (2017): 1480–1490.

55. W. N. Findley and F. A. Davis, *Creep and Relaxation of Nonlinear Viscoelastic Materials* (Courier Corporation, 2013).

56. M. A. Calhoun, S. A. Bentil, E. Elliott, J. J. Otero, J. O. Winter, and R. B. Dupaix, "Beyond Linear Elastic Modulus: Viscoelastic Models for Brain and Brain Mimetic Hydrogels," *ACS Biomaterials Science & Engineering* 5, no. 8 (2019): 3964–3973.

57. M. Rubinstein, R. H. Colby, and Knovel, *Polymer Physics* (Oxford University Press, 2003).

58. M. Rubinstein and A. N. Semenov, "Dynamics of Entangled Solutions of Associating Polymers," *Macromolecules* 34, no. 4 (2001): 1058–1068, https://doi.org/10.1021/ma0013049.

59. M. Rubinstein and S. Panyukov, "Elasticity of Polymer Networks," *Macromolecules* 35 (Aug 2002): 6670–6686, https://doi.org/10.1021/ma0203849.

60. J. Des Cloizeaux, "The Lagrangian Theory of Polymer Solutions at Intermediate Concentrations," *Journal de Physique* 36, no. 4 (1975): 281–291.

61. J. Kim, G. Zhang, M. Shi, and Z. Suo, "Fracture, Fatigue, and Friction of Polymers in Which Entanglements Greatly Outnumber Cross-Links," *Science* 374, no. 6564 (2021): 212–216, https://doi.org/10.1126/science.abg6320.

62. P.-G. de Gennes, *Scaling Concepts in Polymer Physics* (Cornell University Press, 1979).

63. P. J. Flory, *Principles of Polymer Chemistry* (Cornell University Press, 1953).

64. J. D. Ferry, "Viscoelastic Properties of Polymers," (1961).

65. I. Noda, N. Kato, T. Kitano, and M. Nagasawa, "Thermodynamic Properties of Moderately Concentrated-Solutions of Linear-Polymers," *Macromolecules* 14, no. 3 (1981): 668–676.

66. Z. Ma, F. O. Obuseh, B. R. Freedman, J. Kim, M. Torre, and D. J. Mooney, "Integrating Hydrogels and Biomedical Plastics via In Situ Physical Entanglements and Covalent Bonding," *Advanced Healthcare Materials* 14, no. 4 (2025): 2402605, https://doi.org/10.1002/adhm.202402605.

67. Y. Wang, X. Li, X. Zhu, and S.-Q. Wang, "Characterizing State of Chain Entanglement in Entangled Polymer Solutions during and after Large Shear Deformation," *Macromolecules* 45, no. 5 (2012): 2514–2521, https://doi.org/10.1021/ma2024842.

68. Y. Wang and S.-Q. Wang, "Exploring Stress Overshoot Phenomenon Upon Startup Deformation of Entangled Linear Polymeric Liquids," *Journal of Rheology* 53, no. 6 (2009): 1389–1401.

69. H. Wang, D. Zhu, A. Paul et al., "Covalently Adaptable Elastin-Like Protein–Hyaluronic Acid (ELP–HA) Hybrid Hydrogels with Secondary Thermoresponsive Crosslinking for Injectable Stem Cell Delivery," *Advanced Functional Materials* 27, no. 28 (2017), https://doi.org/10.1002/adfm.201605609.

70. N. H. Kalin, "Understanding the Value and Limitations of MRI Neuroimaging in Psychiatry," *American Journal of Psychiatry* 178 (2021): 673–676.

71. M.-F. Chesselet and S. T. Carmichael, "Animal Models of Neurological Disorders," *Neurotherapeutics* 9, no. 2 (2012): 241–244.

72. L. Eliot and S. S. Richardson, "Sex in Context: Limitations of Animal Studies for Addressing Human Sex/Gender Neurobehavioral Health Disparities," *Journal of Neuroscience* 36, no. 47 (2016): 11823–11830.

73. W. Jung, J. Li, O. Chaudhuri, and T. Kim, "Nonlinear Elastic and Inelastic Properties of Cells," *Journal of Biomechanical Engineering* 142, no. 10 (2020): 100806.

74. M. S. Huang, R. S. Navarro, L. G. Brunel et al., "Expanding the Versatility of Dynamic Covalent Hydrogels with Static Covalent Spot-Welding," *Chemistry of Materials* 37, no. 24 (2025): 9758–9774.

75. Z. Gong, S. E. Szczesny, S. R. Caliari et al., "Matching Material and Cellular Timescales Maximizes Cell Spreading on Viscoelastic Substrates," *Proceedings of the National Academy of Sciences of the United States of America* 115, no. 12 (2018): E2686–E2695.

76. C. Huerta-López, A. Clemente-Manteca, D. Velázquez-Carreras et al., "Cell Response to Extracellular Matrix Viscous Energy Dissipation Outweighs High-Rigidity Sensing," *Science Advances* 10, no. 46 (2024): eadf9758.

77. R. A. Suhar, V. M. Doulames, Y. Liu et al., "Hyaluronan and Elastin-Like Protein (HELP) Gels Significantly Improve Microsphere Retention in the Myocardium," *Biomaterials Science* 10, no. 10 (2022): 2590–2608, https://doi.org/10.1039/d1bm01890f.

78. D. Zhang, N. J. Baugh, N. de Paiva Narciso, and S. C. Heilshorn, "Physiological Buffer Selection Alters the Mechanics of Hydrogels with Hydrazone Cross-Links," *Biomacromolecules* 27 (2026): 3222–3236, https://doi.org/10.1021/acs.biomac.5c02684.

79. C. Arshadi, U. Günther, M. Eddison, K. I. Harrington, and T. A. Ferreira, "SNT: A Unifying Toolbox for Quantification of Neuronal Anatomy," *Nature Methods* 18 (Apr 2021): 374–377, https://doi.org/10.1038/s41592-021-01105-7.

80. F. S. Lee, U. N. Nguyen, E. J. Munns, and R. A. Wachs, "Identification of Compounds That Cause Axonal Dieback Without Cytotoxicity in Dorsal Root Ganglia Explants and Intervertebral Disc Cells with Potential to Treat Pain via Denervation," *PLOS ONE* 19, no. 5 (2024): e0300254.

81. B. M. Baker, B. Trappmann, W. Y. Wang et al., "Cell-Mediated Fibre Recruitment Drives Extracellular Matrix Mechanosensing in Engineered Fibrillar Microenvironments," *Nature Materials* 14, no. 12 (2015): 1262–1268.

82. C. M. Madl, B. L. Lesavage, R. E. Dewi et al., "Maintenance of Neural Progenitor Cell Stemness in 3D Hydrogels Requires Matrix Remodelling," *Nature Materials* 16 (2017): 1233–1242, https://doi.org/10.1038/nmat5020.

83. M. Guvendiren, H. D. Lu, and J. A. Burdick, "Shear-Thinning Hydrogels for Biomedical Applications," *Soft Matter* 8 (2012): 260–272.

84. M. Cesaretti, E. Luppi, F. Maccari, and N. Volpi, "A 96-Well Assay for Uronic Acid Carbazole Reaction," *Carbohydrate Polymers* 54 (2003): 59–61, https://doi.org/10.1016/S0144-8617(03)00144-9.

Supporting Information

Additional supporting information can be found online in the Supporting Information section.

Supporting File: adfm76427-sup-0001-SuppMat.pdf.